



Supersonically sprayed Fe₂O₃/C/CNT composites for highly stable Li-ion battery anodes

Chanwoo Park^{a,1}, Edmund Samuel^{a,1}, Bhavana Joshi^b, Taegun Kim^a, Ali Aldalbahi^c, Mohamed El-Newehy^c, Woo Young Yoon^{d,*}, Sam S. Yoon^{a,*}

^a School of Mechanical Engineering, Korea University, Seoul 136-713, Republic of Korea

^b Department of Physics, NES Science College, Swami Ramanand Teerth Marathwada University, Latur Road, Nanded, Maharashtra 431606, India

^c Department of Chemistry, College of Science, King Saud University, Riyadh 11451, Saudi Arabia

^d Department of Materials Science & Engineering, Korea University, Seoul 02841, Republic of Korea

HIGHLIGHTS

- Successful synthesis of Fe₂O₃/C/CNT with stable electrochemical performance.
- Fe₂O₃/C/CNT anode exhibited high discharge capacity (901 mAh·g⁻¹) after 1000 cycles at 1000 mA·g⁻¹.
- Carbon-coating reduced Fe₂O₃ particle size, which increased capacity retention.
- The CNTs intertwined with Fe₂O₃/C nanoparticles to form a 3D network.

ARTICLE INFO

Keywords:

Fe₂O₃
CNT
Lithium-ion battery
Cold spray

ABSTRACT

A synthesized Fe₂O₃/C composite integrated with carbon nanotubes (CNTs) is deposited via cold spraying and used as a highly stable Li-ion battery anode. The X-ray diffraction pattern of the anode material confirms the coexistence of CNTs and mixed Fe₂O₃ phases (α and γ). Morphology and elemental mapping analyses are performed using scanning electron microscopy and transmission electron microscopy, respectively. The Fe₂O₃/C/CNT composite presents the high discharge capacity of 1598 mA·h·g⁻¹ at the current density of 100 mA·g⁻¹. The anode exhibits excellent capacity retention values of 83% and 88% after 100 and 1000 charge–discharge cycles under current densities of 100 and 1000 mA·g⁻¹, respectively. The electrochemical performance of the synthesized Fe₂O₃/C/CNT composite is superior to that of the Fe₂O₃/CNT composite prepared by mixing commercially available Fe₂O₃ and CNTs. This is attributed to the shorter diffusion path of the Li-ions in the relatively smaller Fe₂O₃ particles and faster charge transfer through the highly conductive CNTs.

1. Introduction

The integration of green sustainable energy resources into mobile ambulances, electric vehicles, and advanced portable technologies such as drones requires compact, low-cost, safe, and long-life energy storage devices. Conventional Li-ion batteries (LIBs) with graphite anodes are limited by their low theoretical capacity of 372 mA·h·g⁻¹. [1,2] Their long life cycles, high capacities, and high energy densities suggest that they are promising and reliable energy storage devices. However, the ever-increasing demands for modern portable electronic devices and electric vehicles require batteries with much higher rate performances and power densities. [3] Hence, several metal oxides, including TiO₂,

[4,5] MnO, [6,7] SnO, [8,9] ZnO, [10,11] and FeO_x, [12], bimetallic oxides, including ZnFe₂O₄, [13,14] Zn₂SnO₄, [15,16] and Mn₂SnO₄ [17], composites thereof, and carbides [18–20] have been investigated as anode materials to fulfill the higher energy demands.

Fe₂O₃ is a preferred LIB anode material because of its low cost, eco-friendliness, high theoretical capacity (1007 mA·h·g⁻¹) [21,22], and high conversion capability during lithiation and delithiation. However, in addition to its drawback of low conductivity, Fe₂O₃ experiences a volume expansion of approximately 200% upon lithiation, which leads to pulverization during the electrochemical conversion and restoration process. Jiang et al. reported the use of porous Fe₂O₃ to achieve the capacity of \sim 239 mA·h·g⁻¹ at the current rate of 200 mA·g⁻¹;

* Corresponding authors.

E-mail addresses: wyyoon@korea.ac.kr (W.Y. Yoon), skyoonyoon@korea.ac.kr (S.S. Yoon).

¹ These authors have contributed equally.

furthermore, the achieved capacity retention was 42% after ~ 40 charge–discharge cycles. [23] Sun et al. used Fe_2O_3 nanoparticles as an LIB anode; they reported the first discharge capacity of $772 \text{ mA}\cdot\text{h}\cdot\text{g}^{-1}$ and the capacity retention of $\sim 39\%$ after 50 cycles at the current rate of $100 \text{ mA}\cdot\text{g}^{-1}$. [22] Chen et al. reported using pristine $\alpha\text{-Fe}_2\text{O}_3$ nanoparticles as LIB anodes with the documented first discharge capacity of $1005 \text{ mA}\cdot\text{h}\cdot\text{g}^{-1}$ at the current rate of $200 \text{ mA}\cdot\text{g}^{-1}$; this decreased to $164 \text{ mA}\cdot\text{h}\cdot\text{g}^{-1}$ after 50 cycles. [24] Further reports show similar rapid capacity losses with charge–discharge cycling. [25–27] The extensively researched metal oxides demonstrated that their capacity retentions were limited by the two significant factors of their low conductivity and their irreversible morphological changes, caused by volume expansion and contraction during the insertion and extraction of Li ions, which are also referred to as lithiation (discharging) and delithiation (charging), respectively.

Hence, synthesizing novel composites is necessary to achieve superior capacity retention during long-term cycling. Therefore, the present study focuses on demonstrating the superior performance of a synthesized $\text{Fe}_2\text{O}_3/\text{C}/\text{CNT}$ composite compared to that of a composite ($\text{Fe}_2\text{O}_3/\text{CNT}$) prepared by mixing commercially available Fe_2O_3 and CNTs. All samples were deposited via non-vacuum and supersonic deposition techniques. Cold spraying is an emerging technique for the rapid and uniform deposition of nanomaterials on both flexible and non-flexible substrates. [28] The method is scalable and applicable in roll-to-roll processing; it is thus economically viable. Because of the high-speed impact of the particles onto the substrate, the bonding energy is substantial, resulting in good adhesion between the deposited materials and the substrate. [29–33] Fe_2O_3 particles smaller than those commercially available were successfully synthesized, thus downscaling the active material to achieve faster Li^+ diffusion. Thus, the $\text{Fe}_2\text{O}_3/\text{C}/\text{CNT}$ composite presented a superior energy storage capacity and improved stable electrochemical performance as an LIB anode.

2. Experimental

2.1. Materials

Iron(III) chloride hexahydrate ($\text{FeCl}_3\cdot 6\text{H}_2\text{O}$), polyvinylpyrrolidone (PVP, $M_w = 40 \text{ kDa}$), and CNTs were purchased from Sigma-Aldrich for the synthesis of $\text{Fe}_2\text{O}_3/\text{C}/\text{CNT}$. Fe_2O_3 particles ($> 99\%$), polyacrylonitrile (PAN, $M_w = 150 \text{ kDa}$) used as a dispersant, and *N,N*-dimethylformamide (DMF) as the solvent were also purchased from Sigma-Aldrich (Korea). All chemicals were used as purchased without further purification.

2.2. Chemical synthesis of $\text{Fe}_2\text{O}_3/\text{C}/\text{CNT}$

The steps for the synthesis of $\text{Fe}_2\text{O}_3/\text{C}/\text{CNT}$ are presented in Scheme 1. First, 0.1 g of CNTs were dispersed in 50 mL deionized (DI) water under ultrasonication for 10 min. Afterward, $\text{FeCl}_3\cdot 6\text{H}_2\text{O}$ was added to the CNT dispersion and the mixture was stirred vigorously to ensure the proper mixing of FeCl_3 . The prepared solution of PVP and 2 mL of 0.5 M KOH were added to the FeCl_3 -CNT mixture under continuous stirring for 30 min. The KOH solution was used to generate Fe_2O_3 particles, while the presence of PVP ensured that particle growth and

agglomeration were restricted. After 30 min, the beaker was tightly closed using Al foil and then heated at 80°C for 2 h. Then, the solution was cooled to room temperature (RT, 20°C). The formed $\text{Fe}_2\text{O}_3/\text{C}/\text{CNT}$ was filtered via centrifugation and washed three times with DI water. The separated $\text{Fe}_2\text{O}_3/\text{C}/\text{CNT}$ particles were dried at 100°C in a vacuum for 1 h to ensure humidity removal.

2.3. Deposition of CNT, Fe_2O_3 , $\text{Fe}_2\text{O}_3/\text{CNT}$ and $\text{Fe}_2\text{O}_3/\text{C}/\text{CNT}$

The CNT, Fe_2O_3 , $\text{Fe}_2\text{O}_3/\text{CNT}$, and $\text{Fe}_2\text{O}_3/\text{C}/\text{CNT}$ particles were deposited on Cu foil by the cold spraying technique. We prepared eight solutions of 40 mL DMF (solvent) and 0.3 mL 8 wt% PAN solution (solute). Subsequently, 3 g PVP, 0.8 g of pristine CNTs, 1.2, 1.4, 1.6, and 1.8 g Fe_2O_3 , 0.8 g CNTs with 1.6 g Fe_2O_3 , and 0.2 g synthesized $\text{Fe}_2\text{O}_3/\text{C}/\text{CNT}$ were added to different containers of the DMF/PAN solutions. All mixtures were stirred vigorously for 30 min followed by tip sonication for 40 s to obtain well-dispersed mixtures, which were then placed in syringes.

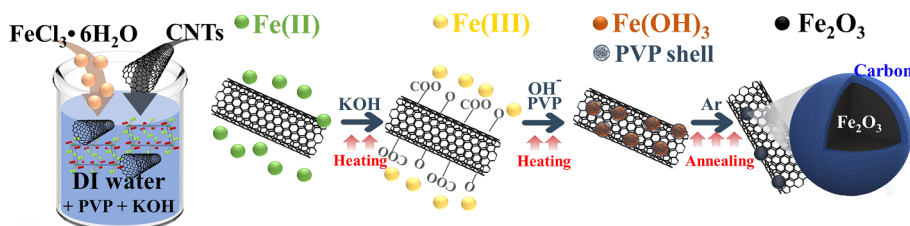
Each prepared mixture was introduced into an atomizer at a constant flow rate using the syringe pump. The fluid sprayed by the atomizer was deposited on Cu foil under the supersonic impact of the cold spray, as illustrated in Fig. 1. The cold-spray coating unit comprised a supersonic nozzle, x-y stage, atomizer, compressor, and an inline heater. The cold-spray system and coating deposition process have been described in detail in previously published papers. [34,35] The deposition conditions used in this study are summarized in Table 1. The cold-sprayed films were annealed in Ar atmosphere at 500°C for 60 min at a ramp rate of $3^\circ\text{C}/\text{min}$.

2.4. Physicochemical characterization

The crystal phases of the CNTs, Fe_2O_3 , $\text{Fe}_2\text{O}_3/\text{CNT}$, and $\text{Fe}_2\text{O}_3/\text{C}/\text{CNT}$ particles were analyzed using a SmartLab (Rigaku) X-ray diffraction (XRD) instrument. Raman spectra were obtained using an NRS-3100 (Jasco) spectrometer featuring a high-performance 532-nm laser and an 1800-grooves/nm holographic grating. The structural morphologies of the CNTs, Fe_2O_3 , $\text{Fe}_2\text{O}_3/\text{CNT}$, and $\text{Fe}_2\text{O}_3/\text{C}/\text{CNT}$ particles were observed using an S-5000 (Hitachi, Ltd.) field-emission scanning electron microscopy (FE-SEM) device and a JEM 2100F (JEOL Inc.) transmission electron microscopy (TEM) apparatus. High-angle annular dark-field scanning transmission electron microscopy measurements were performed for elemental mapping. The presence of the elements and their chemical states were determined using a theta probe (Thermo Fisher Scientific Co.) X-ray photoelectron spectroscopy (XPS) base system. The N_2 adsorption and desorption isotherms of the samples were measured by a Micrometric Tristar II 3020 instrument and Brunauer–Emmett–Teller (BET) analyses were performed to analyze the surface areas of the fabricated films.

2.5. Electrochemical characterization

The annealed CNTs, Fe_2O_3 , $\text{Fe}_2\text{O}_3/\text{CNT}$, and $\text{Fe}_2\text{O}_3/\text{C}/\text{CNT}$ samples deposited on Cu foil were punched into 1.54-cm^2 discs. The electrode was lithiated from 3 to 0.01 V and delithiated from 0.01 to 3 V under various current densities. The current density was defined as the ratio of the applied current [mA] to the active material mass [g]; thus, its unit is



Scheme 1. Synthesis of $\text{Fe}_2\text{O}_3/\text{C}/\text{CNT}$ composite particles from $\text{FeCl}_3\cdot 6\text{H}_2\text{O}$. Here, CNTs, DI water, and PVP indicate carbon nanotubes, deionized water, and polyvinylpyrrolidone, respectively.

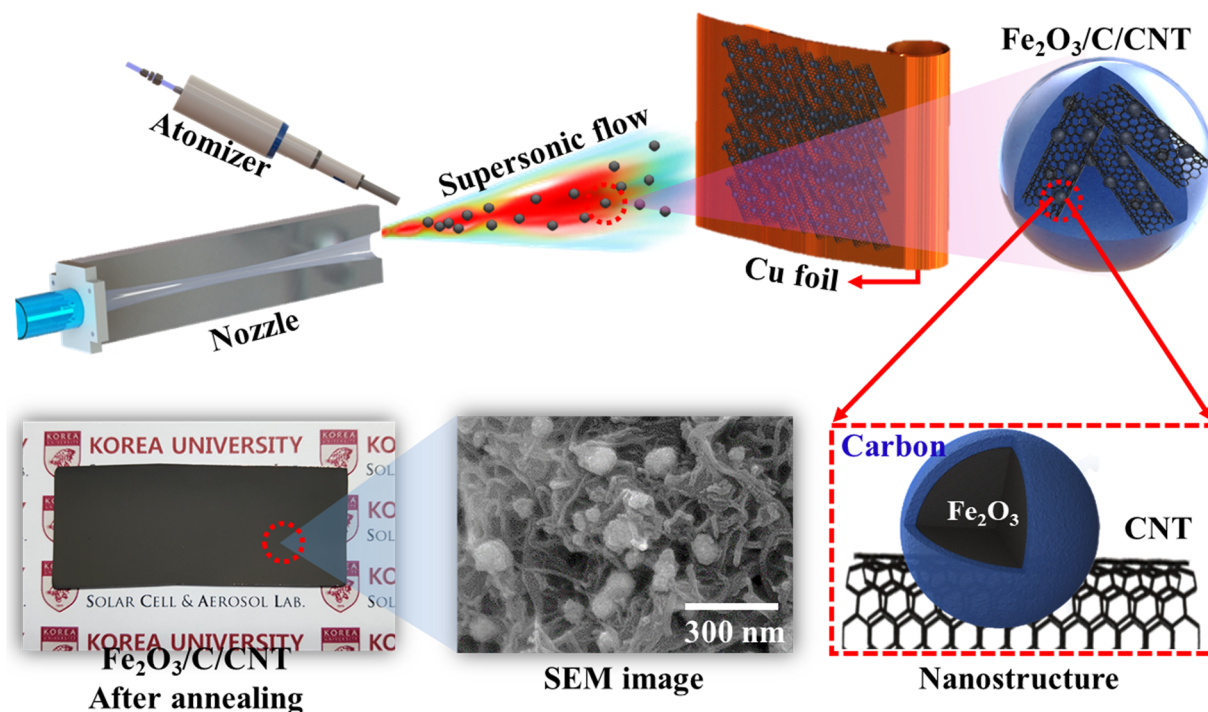


Fig. 1. Schematic of supersonic spray setup, film deposition on Cu foil, and morphology of $\text{Fe}_2\text{O}_3/\text{C}/\text{CNT}$ film. Here, CNT and SEM denote carbon nanotube and scanning electron microscopy, respectively.

Table 1

Operating conditions of supersonic cold-spray during coating.

Spraying parameter	Values
Pressure (P_0) [bar]	4
Heater temperature [$^{\circ}\text{C}$]	250
Flowrate [ml/min]	1.5
Traverse speed [mm/s]	15
Spraying distance [mm]	150
Number of passes	10

[$\text{mA}\cdot\text{g}^{-1}$]. The specific capacity is the product of the specific current and the time required for charging or discharging; thus, its unit is [$\text{mA}\cdot\text{h}\cdot\text{g}^{-1}$]. The active material mass was estimated by subtracting the current collector mass (0.0341 g) from the total electrode mass (the active material and the current collector mass). The active material mass for the CNT sample was 1 mg while that for the Fe_2O_3 , $\text{Fe}_2\text{O}_3/\text{CNT}$, and $\text{Fe}_2\text{O}_3/\text{C}/\text{CNT}$ samples was 1.4 mg. The punched discs were used as the working electrodes, and 16-mm-diameter Li foil discs were used as the reference electrodes in CR2032-type coin cells. The electrodes were electrically insulated using Celgard 2400 polymer membranes (Celgard, Chungbuk, South Korea) as separators. In addition, 1-M LiPF_6 solution in ethylene carbonate, dimethyl carbonate, and ethyl methyl carbonate (1:1:1 v/v/v) (PuriEL, Soulbrain, Seongnam, South Korea) was used as the electrolyte. The open-circuit voltage of the assembled half-cells for all the samples was measured as 3 V. Therefore, considering the open-circuit voltage and the deintercalation/oxidation process, the galvanostatic measurements were performed in the potential window of 0.01–3 V at 25 $^{\circ}\text{C}$ because the deintercalation or oxidation of Li-ions relative to Fe_2O_3 is completed between 2 and 2.5 V. [24,36] The galvanostatic measurements were performed using a WBCS3000 (WonATech, Seoul, South Korea) battery cyler system for long cycles at the constant current densities of 100 and 1000 $\text{mA}\cdot\text{g}^{-1}$. Half-cells were subjected to current rate tests at 100, 200, 500, and 1000 $\text{mA}\cdot\text{g}^{-1}$. Furthermore, electrochemical impedance spectroscopy (EIS) measurements were performed in the frequency range of 100 kHz

to 0.01 Hz using a VersaSTAT-3 (Princeton Applied Research, USA) potentiostat with a small perturbation voltage of 10 mV.

3. Results and discussion

3.1. Material properties

The XRD patterns of the pristine CNTs and Fe_2O_3 -based composite samples deposited via supersonic cold-spraying are illustrated in Fig. 2a. Characteristic diffraction peaks at 25.8 $^{\circ}$ and 43.5 $^{\circ}$ are observed in the XRD profile of the CNT sample. The peaks at 38 $^{\circ}$, 44 $^{\circ}$, and 50.2 $^{\circ}$ are ascribed to the Cu substrate. The XRD patterns of the Fe_2O_3 and $\text{Fe}_2\text{O}_3/\text{CNT}$ samples exhibit diffraction peaks at 24.2 $^{\circ}$, 33.2 $^{\circ}$, 35.5 $^{\circ}$, 40.9 $^{\circ}$, 43.6 $^{\circ}$, 49.4 $^{\circ}$, 54.1 $^{\circ}$, 57.1 $^{\circ}$, 62.5 $^{\circ}$, and 71.9 $^{\circ}$, corresponding to α - Fe_2O_3 (hematite), while the peaks at 30.1 $^{\circ}$, 43.2 $^{\circ}$, 64.0 $^{\circ}$, and 74.1 $^{\circ}$ represent γ - Fe_2O_3 (maghemite). Similarly, mixed γ - Fe_2O_3 and α - Fe_2O_3 phases are observed in the XRD pattern of the synthesized $\text{Fe}_2\text{O}_3/\text{C}/\text{CNT}$ composite sample. The peaks at 33.2 $^{\circ}$, 35.3 $^{\circ}$, 39.4 $^{\circ}$, and 43.4 $^{\circ}$ are attributed to the (1 0 4), (1 1 0), (0 0 6), and (2 0 2) planes of α - Fe_2O_3 , respectively, whereas the peaks at 14.0 $^{\circ}$, 18.3 $^{\circ}$, 26.8 $^{\circ}$, 56.2 $^{\circ}$, 61.2 $^{\circ}$, 64.4 $^{\circ}$, and 74.2 $^{\circ}$ corresponded to the (1 1 0), (1 1 1), (2 1 1), (5 1 1), (5 2 1), (4 4 1), and (5 3 3) planes of γ - Fe_2O_3 , respectively. The diffraction peaks of α - Fe_2O_3 and γ - Fe_2O_3 matched the JCPDS cards 24-0072 and 39-1346, respectively, and are marked using “●” and “▼” symbols in Fig. 2a. [37,38] By using the Scherrer equation of $\tau = K\lambda/(\beta\theta)$ and the peak values from the XRD pattern, the crystallite size τ can be determined. The dimensionless constant of $K = 0.9$ is used. λ is the X-ray wavelength. β is the full-width half maximum of line-broadening. θ is the Bragg angle. Thus, the estimated crystallite sizes of the Fe_2O_3 , $\text{Fe}_2\text{O}_3/\text{CNT}$, and $\text{Fe}_2\text{O}_3/\text{C}/\text{CNT}$ samples are 52.3, 62.3, and 10.7 nm, respectively. The γ - Fe_2O_3 phase presents Fe^{2+} vacancies at the octahedral sites, which are beneficial for the insertion of Li-ions.

The Raman spectra of the CNT, Fe_2O_3 , $\text{Fe}_2\text{O}_3/\text{CNT}$, and $\text{Fe}_2\text{O}_3/\text{C}/\text{CNT}$ samples are presented in Fig. 2b. The peaks at 1347, 1596, and 2692 cm^{-1} correspond to the carbon defect band (D), graphitic carbon (G) band, and the 2D band of the CNTs. These bands are not observed in

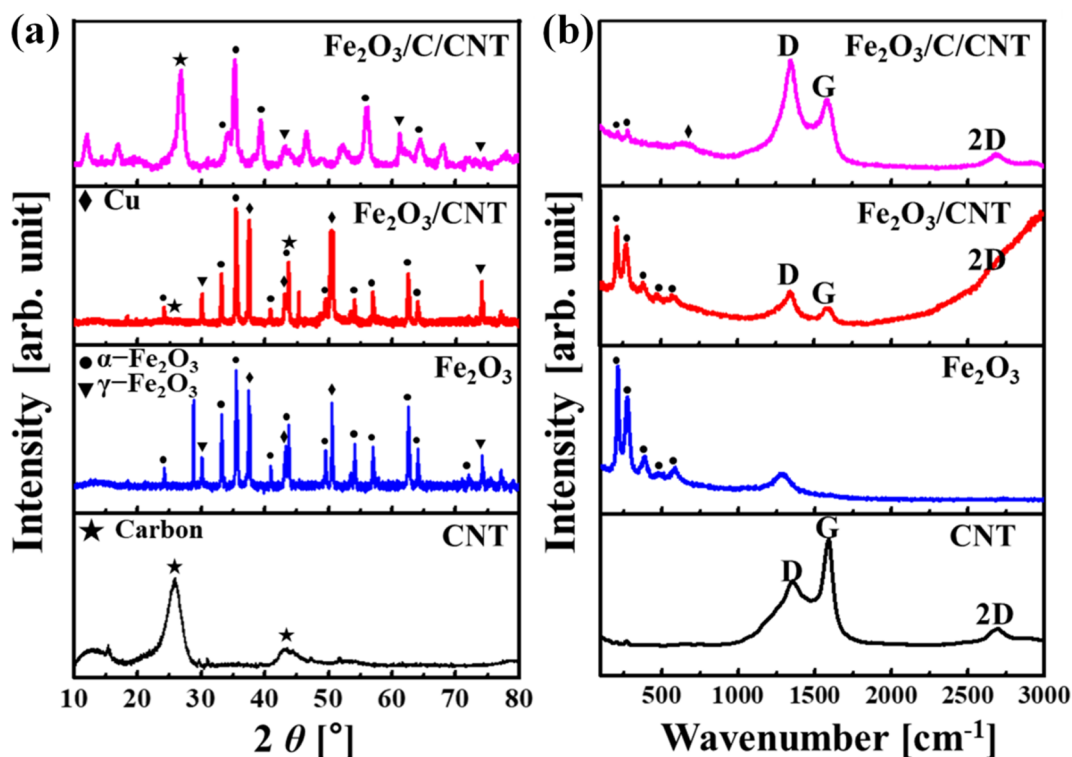


Fig. 2. (a) X-ray diffraction patterns and (b) Raman spectra of carbon nanotubes (CNTs), Fe_2O_3 , $\text{Fe}_2\text{O}_3/\text{CNT}$, and $\text{Fe}_2\text{O}_3/\text{C}/\text{CNT}$.

the spectrum of the Fe_2O_3 sample because this sample lacks CNTs. For the pristine CNT sample, the G band is more prominent than the D band, and the 2D band is sharp and distinct. However, the D bands are predominant in the spectra of $\text{Fe}_2\text{O}_3/\text{CNT}$ and $\text{Fe}_2\text{O}_3/\text{C}/\text{CNT}$, indicating that the CNT walls achieve good adhesion with the Fe_2O_3 particles. The I_D/I_G ratios for the CNT, $\text{Fe}_2\text{O}_3/\text{CNT}$ and $\text{Fe}_2\text{O}_3/\text{C}/\text{CNT}$ samples are estimated as 0.68, 1.43, and 1.4, respectively, according to Fig. 2b. The G band is absent in the Raman spectrum for Fe_2O_3 ; therefore, its I_D/I_G ratio cannot be estimated. The linkage between the CNTs and Fe_2O_3 particles in the $\text{Fe}_2\text{O}_3/\text{CNT}$ sample can be attributed to the supersonic impact during deposition, which may reduce the graphitic state of the CNTs, thus yielding a strong D band in the spectrum. However, the adhesion of CNTs and $\text{Fe}_2\text{O}_3/\text{C}/\text{CNT}$ begin during the particle synthesis process; therefore, the defects occurring in the CNT structure are milder than those observed in the structure of the $\text{Fe}_2\text{O}_3/\text{CNT}$ sample. The Raman spectra of Fe_2O_3 and $\text{Fe}_2\text{O}_3/\text{CNT}$ exhibit five phonon modes related to the α - and γ - Fe_2O_3 phases in the wavenumber range $100\text{--}800\text{ cm}^{-1}$: two A_{1g} modes corresponding to the peaks at 216 and 493 cm^{-1} , and three E_g modes indicated by peaks at 282 , 399 , and 594 cm^{-1} . [39,40] However, the intensity of the Fe_2O_3 peaks in the spectrum of the $\text{Fe}_2\text{O}_3/\text{C}/\text{CNT}$ sample is lower, which is attributed to the C coating from the carbonization of PVP. The two peaks of Fe_2O_3 at 217 and 284 cm^{-1} correspond to the A_{1g} and E_g modes, respectively. Furthermore, the Raman spectrum of $\text{Fe}_2\text{O}_3/\text{C}/\text{CNT}$ presents a broad hump at approximately 720 cm^{-1} , which is attributed to the local Fe–O structures around the cation vacancies in γ - Fe_2O_3 ; this is consistent with the XRD data.

Fig. 3 depicts the scanning electron microscopy (SEM) images of the annealed CNT, Fe_2O_3 , $\text{Fe}_2\text{O}_3/\text{CNT}$, and $\text{Fe}_2\text{O}_3/\text{C}/\text{CNT}$ samples at different magnifications. The presences of CNTs, mixed Fe_2O_3 phases, intertwined CNTs, and Fe_2O_3 in the structure of $\text{Fe}_2\text{O}_3/\text{CNT}$ and $\text{Fe}_2\text{O}_3/\text{C}/\text{CNT}$ are already confirmed using XRD analysis (Fig. 2a). The CNT and Fe_2O_3 particles are well distributed over the Cu foil, along with voids, which may facilitate better interfacing between the electrode and electrolyte surface (Fig. 3a and c). The agglomeration and large size of the Fe_2O_3 particles can be observed in Fig. 3d–i. The larger Fe_2O_3

particles undergo consistent pulverization during electrochemical reactions, such as the lithiation and delithiation processes because of the volume expansion and contraction of the Fe_2O_3 particles. The breakage of Fe_2O_3 particles caused by volume expansion and contraction not only deteriorates the performance of the Fe_2O_3 anode but also breaks the solid electrolyte interface (SEI) layer, which causes more irreversible reactions and consequently reduces the effect of the intertwined CNTs. Thus, it is necessary to control the size of the Fe_2O_3 particles. Consequently, the $\text{Fe}_2\text{O}_3/\text{C}/\text{CNT}$ sample is synthesized via precipitation using PVP as a capping agent. The synthesized Fe_2O_3 particles adhering to the CNTs are smaller (Fig. 3j–l) than the pristine Fe_2O_3 particles (Fig. 3d–i). The agglomeration of the Fe_2O_3 particles is significantly decreased by the presence of C from the carbonized PVP deposited on their surfaces (Fig. 3j–l). The average thicknesses of the CNT, Fe_2O_3 , $\text{Fe}_2\text{O}_3/\text{CNT}$, and $\text{Fe}_2\text{O}_3/\text{C}/\text{CNT}$ films are 4.5 , 7.2 , 11.7 , and $4.5\text{ }\mu\text{m}$, respectively, based on the cross-sectional views shown in Fig. S1. The concentrations of the elements (Fe, O, C and N) for all samples are determined using energy-dispersive X-ray spectroscopy and SEM data, and the results are summarized in Table 2.

We used TEM analysis to confirm the morphology of the $\text{Fe}_2\text{O}_3/\text{C}/\text{CNT}$ particles (Fig. 4). The low-magnification TEM image (Fig. 4a) indicates that the CNTs and $\text{Fe}_2\text{O}_3/\text{C}$ particles are intertwined. The characteristic lattice fringes of $\text{Fe}_2\text{O}_3/\text{C}/\text{CNT}$ are observed in the high-resolution TEM image in Fig. 4b. The $\text{Fe}_2\text{O}_3/\text{C}$ nanoparticles are well-adhered to the CNTs. Fig. 4c illustrates the selected-area electron diffraction (SAED) pattern, showing the diffraction rings for the $(1\ 1\ 6)$, $(3\ 1\ 1)$, and $(1\ 0\ 4)$ planes of the α - Fe_2O_3 phase. Furthermore, the elemental mapping images (see Fig. 4d) of $\text{Fe}_2\text{O}_3/\text{C}/\text{CNT}$ confirm the presences of C, Fe, and O in the sample. Fig. S2a illustrates the high-magnification TEM image of the $\text{Fe}_2\text{O}_3/\text{C}/\text{CNT}$ sample, in which the CNT and Fe_2O_3 particles are marked. Moreover, Fig. S2a shows the C coating over the Fe_2O_3 particles. Thus, the presence of C restricts the size of the Fe_2O_3 particles and significantly reduces agglomeration compared to the $\text{Fe}_2\text{O}_3/\text{CNT}$ sample (see Fig. 3). The overlapped elemental mapping images of C and Fe are presented in Fig. S2b and indicate that the Fe_2O_3 particles are well coated with C. Moreover, the

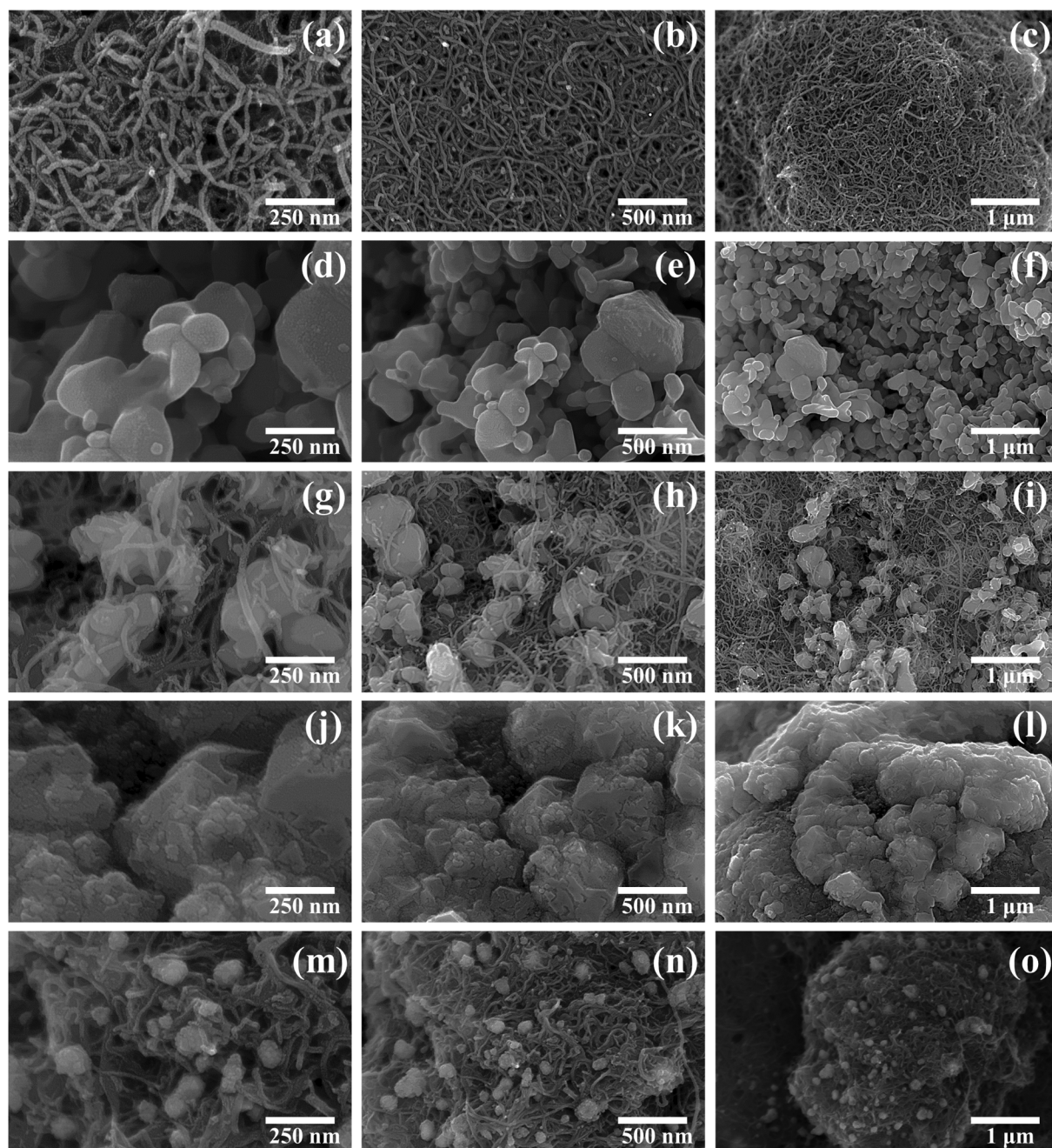


Fig. 3. Scanning electron microscopy images of (a)-(c) carbon nanotubes (CNTs), (d)-(f) Fe_2O_3 , (g)-(i) $\text{Fe}_2\text{O}_3/\text{CNT}$, and (j)-(l) $\text{Fe}_2\text{O}_3/\text{C}/\text{CNT}$.

Table 2
Element weight percentages of Fe-based composite films.

Element Case	Fe	C	O	N
	wt%	wt%	wt%	wt%
CNT	–	89.75	7.48	2.77
Fe_2O_3	48.12	15.10	36.34	0.44
$\text{Fe}_2\text{O}_3/\text{CNT}$	42.19	38.81	19.00	–
$\text{Fe}_2\text{O}_3/\text{C}/\text{CNT}$	7.36	71.93	12.28	8.42

adherence of $\text{Fe}_2\text{O}_3/\text{C}$ to the CNTs is observed.

The oxidation states and chemical composition of the $\text{Fe}_2\text{O}_3/\text{C}/\text{CNT}$ composite were identified using XPS analysis. The XPS survey profile of $\text{Fe}_2\text{O}_3/\text{C}/\text{CNT}$ (Fig. 5a) confirms the presences of Fe, O, and C in the sample. The deconvoluted C 1 s core spectrum (Fig. 5b) exhibits two

peaks at 284.6 and 286.5 eV. The peak at 284.6 eV is assigned to the C–C (sp^2) bonds of the CNTs; that at 286.5 eV is ascribed to the C–O bonds. The intensity of the C–O peak is lower than that of the C–C one, suggesting that the O-containing functional groups are removed during annealing. The high-resolution Fe 2p spectrum (Fig. 5c) presents two apparent peaks at 710.4 and 724.1 eV, which are attributed to Fe $2p_{3/2}$ and Fe $2p_{1/2}$, respectively, and their binding energy separation is ~ 13.7 eV. This implies the presence of the Fe^{3+} state, which is consistent with the presence of the Fe_2O_3 phase. The peak at 710.8 eV is deconvoluted into two peaks at 710.5 and 712.5 eV plus a satellite peak at 717.5 eV, which also confirm the presence of Fe^{3+} ions. The high-resolution O 1 s spectrum (Fig. 5d) can be deconvoluted into two O contributions. The peaks at 529.6 and 532 eV correspond to Fe–O and Fe–O–H, respectively; the O–H groups originate from the moisture chemisorbed on the surface of the $\text{Fe}_2\text{O}_3/\text{C}/\text{CNT}$ composite.

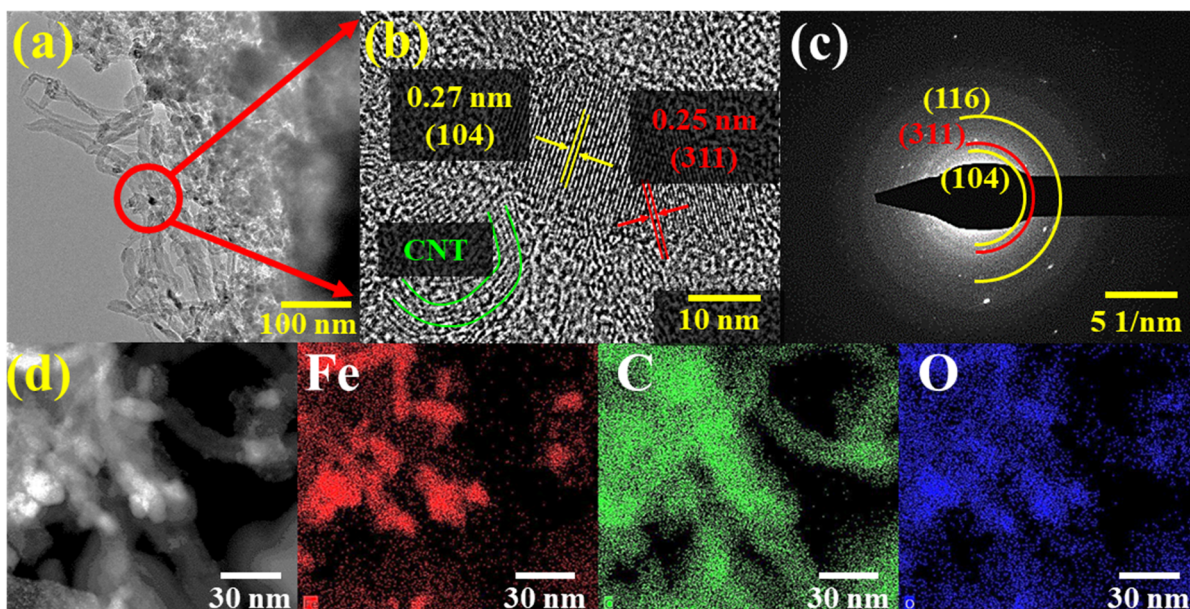


Fig. 4. (a) Transmission electron microscopy image, (b) high-resolution transmission electron microscopy image, and (c) selected-area electron diffraction pattern of $\text{Fe}_2\text{O}_3/\text{CNT}$. (d) High-angle annular dark-field imaging scanning transmission electron microscopy image of mapping area and elemental mapping images of Fe, C, and O.

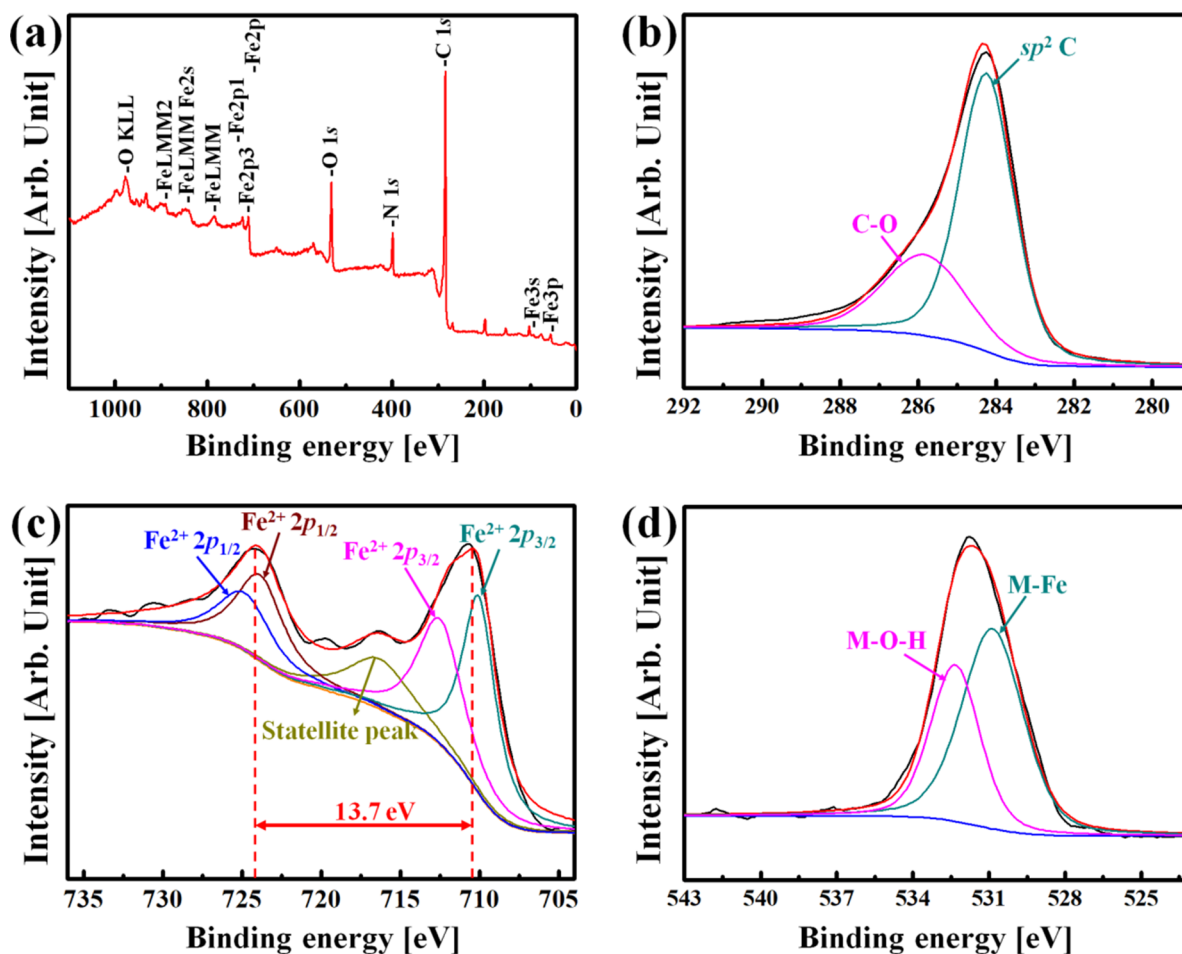


Fig. 5. (a) X-ray photoelectron spectroscopy (XPS) survey profile of $\text{Fe}_2\text{O}_3/\text{CNT}$ and core XPS profiles of (b) C, (c) Fe, and (d) O. Here CNTs are carbon nanotubes.

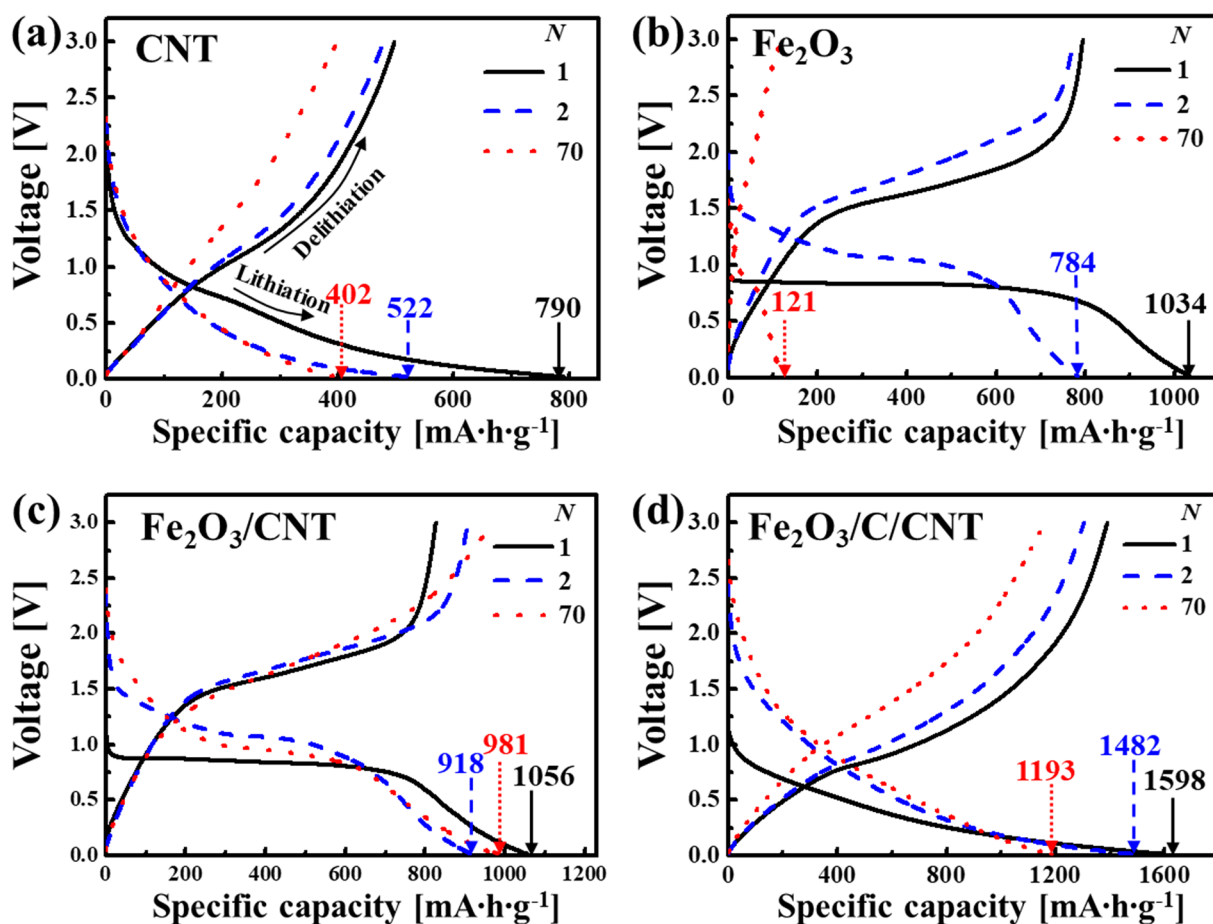


Fig. 6. Discharge-charge profiles of (a) CNT, (b) Fe_2O_3 , (c) $\text{Fe}_2\text{O}_3/\text{CNT}$, and (d) $\text{Fe}_2\text{O}_3/\text{C}/\text{CNT}$ anodes at the 1st, 2nd, and 70th cycles; the current rate is $100 \text{ mA}\cdot\text{g}^{-1}$.

3.2. Electrochemical performance

The discharge-charge profiles of CNT, Fe_2O_3 , $\text{Fe}_2\text{O}_3/\text{CNT}$, and $\text{Fe}_2\text{O}_3/\text{C}/\text{CNT}$ for the 1st, 2nd, and 70th cycles at the current rate of $100 \text{ mA}\cdot\text{g}^{-1}$ are presented in Fig. 6. The coulombic efficiency (CE) values of CNT, Fe_2O_3 , $\text{Fe}_2\text{O}_3/\text{CNT}$, and $\text{Fe}_2\text{O}_3/\text{C}/\text{CNT}$ for the first cycle are 63%, 77%, 78%, and 87%, respectively. The level of N_2 adsorption at $P/P_0 = 1$ for the CNTs was approximately $800 \text{ cm}^3\cdot\text{g}^{-1}$, as shown in Fig. S3a. The corresponding surface area of the CNT film was $223 \text{ m}^2\cdot\text{g}^{-1}$ based on BET analysis. This high surface area promotes rapid Li^+ diffusion. In contrast, an electrolyte readily permeates the nanosized cavities of the CNTs, which leads to SEI formation, yielding the relatively high irreversible capacity loss of $292 \text{ mA}\cdot\text{h}\cdot\text{g}^{-1}$. This high loss is attributed to both the SEI layer formation and the trapping of Li^+ within the CNT core. Note that the measured discharge capacity comprises the charge capacity and the irreversible capacity loss. For the CNT case in Fig. 6a, the measured discharge capacity is $790 \text{ mA}\cdot\text{h}\cdot\text{g}^{-1}$, which is the sum of the charge capacity of $498 \text{ mA}\cdot\text{h}\cdot\text{g}^{-1}$ and the irreversible capacity loss of $292 \text{ mA}\cdot\text{h}\cdot\text{g}^{-1}$. Because the CE is defined as the ratio of the charge to discharge capacity, the charge capacity is estimated as $(0.63)\cdot(790) = 498 \text{ mA}\cdot\text{h}\cdot\text{g}^{-1}$ for the CNT case. Then the irreversible capacity loss is the difference between the discharge and charge capacity, which is $292 \text{ mA}\cdot\text{h}\cdot\text{g}^{-1}$. [41–43] This high loss level for the CNT case is attributed to the CNTs' inability to achieve Li^+ deintercalation from the inner cores of the CNTs, related to the high surface areas of the CNTs. [44] Based on the BET analysis, the surface areas of the Fe_2O_3 , $\text{Fe}_2\text{O}_3/\text{CNT}$, and $\text{Fe}_2\text{O}_3/\text{C}/\text{CNT}$ samples are 6, 44, and $86 \text{ m}^2\cdot\text{g}^{-1}$, respectively, which are significantly lower than that of the CNT sample. Therefore, relatively higher CE values of 77, 78, and 87% are observed for the Fe_2O_3 , $\text{Fe}_2\text{O}_3/\text{CNT}$, and $\text{Fe}_2\text{O}_3/\text{C}/\text{CNT}$

samples, respectively. Note that these capacity values are from $N = 1$ after the first discharge/charge cycle; see Fig. 6. The irreversible capacity loss of the Fe_2O_3 sample was $238 \text{ mA}\cdot\text{h}\cdot\text{g}^{-1}$, attributed to the SEI layer formation alone. However, in the presence of CNTs, the effect of Li^+ trapping within the CNT cores also contributes to capacity loss, as in the pure CNT, $\text{Fe}_2\text{O}_3/\text{CNT}$, and $\text{Fe}_2\text{O}_3/\text{C}/\text{CNT}$ samples. The irreversible capacity losses of the $\text{Fe}_2\text{O}_3/\text{CNT}$ and $\text{Fe}_2\text{O}_3/\text{C}/\text{CNT}$ samples at $N = 1$ are 229 and $208 \text{ mA}\cdot\text{h}\cdot\text{g}^{-1}$, respectively.

The first reversible discharge capacity and retained capacity values are illustrated in Fig. 6 for all samples. The differences between the CNT and Fe_2O_3 samples are observed in Fig. 6a and b, and it can be inferred that C, as the active material, prevents a decrease in the retained capacity. However, because Fe_2O_3 undergoes consistent volume expansion and contraction, which causes its pulverization, its reversible discharge capacity after 70 cycles is significantly smaller (by $\sim 88\%$) than that after the first cycle. The retained capacity of the $\text{Fe}_2\text{O}_3/\text{CNT}$ sample ($981 \text{ mA}\cdot\text{h}\cdot\text{g}^{-1}$, Fig. 6c) is significantly higher than that of Fe_2O_3 ($121 \text{ mA}\cdot\text{h}\cdot\text{g}^{-1}$, Fig. 6b). Moreover, the capacity of $\text{Fe}_2\text{O}_3/\text{C}/\text{CNT}$ is higher than that of the CNT sample (Fig. 6a). However, the first reversible discharge capacities of CNT and Fe_2O_3 both include larger irreversible capacities. The capacity losses can be attributed to the irreversible formation of the Li_xC_y complex and Li_2O product for the CNT and Fe_2O_3 samples, respectively. The capacity loss of the Fe_2O_3 sample can also be attributed to the thick SEI that covers the pulverized Fe_2O_3 particles. The discharge curves for the CNT and $\text{Fe}_2\text{O}_3/\text{C}/\text{CNT}$ samples indicate that their specific capacity values are gradually increased as the voltage is decreased. For the CNT sample, only intercalation occurs; therefore, no plateau region is observed. However, a negligible hump is observed at approximately 0.7 V (Fig. 6a), which can be attributed to the formation of the SEI layer. However, no plateau or hump is

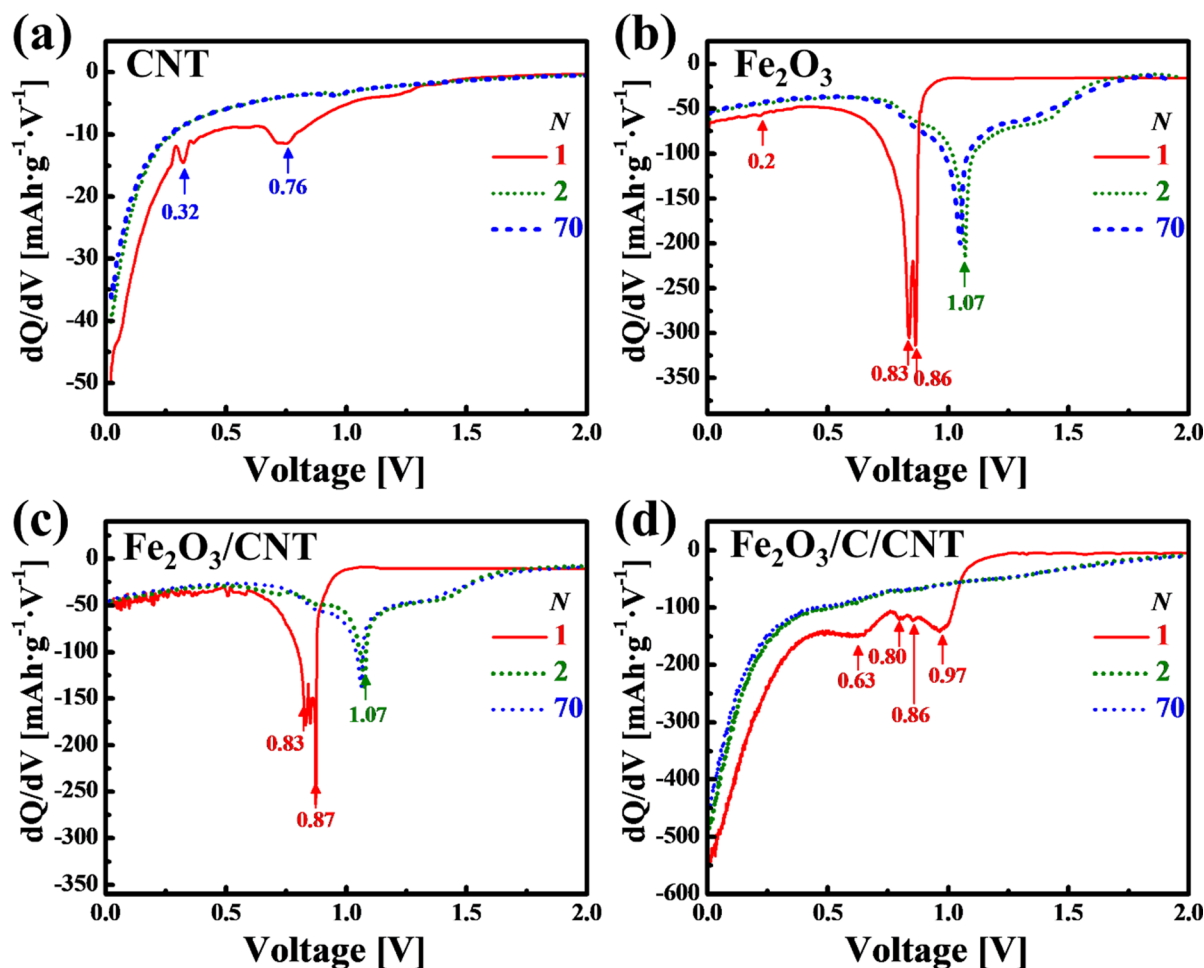


Fig. 7. Differential capacity curves of (a) CNT, (b) Fe_2O_3 , (c) $\text{Fe}_2\text{O}_3/\text{CNT}$, and (d) $\text{Fe}_2\text{O}_3/\text{C}/\text{CNT}$ samples during discharge (lithiation). Here N is the number of cycles.

observed in the discharge/charge profile of the $\text{Fe}_2\text{O}_3/\text{C}/\text{CNT}$ sample (Fig. 6d). This may indicate the formation of a thin SEI layer and the very slow reduction of Fe_2O_3 , which suggests that the Fe_2O_3 particles are well covered by C. This suggestion is consistent with the morphological characterization performed using TEM and elemental mapping analysis (Fig. S1a and b). The Fe_2O_3 and $\text{Fe}_2\text{O}_3/\text{CNT}$ samples contain the as-purchased Fe_2O_3 particles. At the voltage of ~ 0.86 V, the Fe^{3+} ions in these samples are rapidly reduced to Fe^{2+} , as indicated by the very flat plateau regions in Fig. 6b and c. However, the crystalline structure of Fe_2O_3 changes after the first cycle, and the plateau is shifted to ~ 1.1 V. [45] The almost overlapping discharge profiles for the 2nd and 70th cycles indicates the stable electrochemical performances of the CNT, $\text{Fe}_2\text{O}_3/\text{CNT}$, and $\text{Fe}_2\text{O}_3/\text{C}/\text{CNT}$ samples. [36]

The differential capacities of the CNT, Fe_2O_3 , $\text{Fe}_2\text{O}_3/\text{CNT}$, and $\text{Fe}_2\text{O}_3/\text{C}/\text{CNT}$ samples are analyzed, and the results are presented in Fig. 7. The changes in the differential capacity indicate the phase changes experienced by Fe_2O_3 and its composites during the discharge or lithiation electrochemical reactions of the anode (for the half-cell). The peaks at 0.32 and 0.76 V marked in Fig. 7a are ascribed to the intercalation of Li^+ into the CNTs and the formation of the SEI layer, respectively. [46] Fig. 7b and c depict two sharp peaks at 0.86 and 0.83 V, which correspond to the conversion of the α - and γ - Fe_2O_3 phases to $\text{Li}_x\text{Fe}_2\text{O}_3$ and the subsequent conversion of $\text{Li}_x\text{Fe}_2\text{O}_3$ to Fe and Li_2O at the low voltage of ~ 0.2 V. The presence of these two close peaks confirms the presence of mixed α - and γ - Fe_2O_3 phases, in agreement with the XRD pattern of the starting material. The conversion of α - and γ - Fe_2O_3 to $\text{Li}_x\text{Fe}_2\text{O}_3$ at ~ 0.86 V is consistent with the discharge profiles illustrated in Fig. 6b and c. The peak of the

differential capacity curves of Fe_2O_3 and $\text{Fe}_2\text{O}_3/\text{CNT}$ for $N = 2$ (N is the number of cycles) is shifted to ~ 1.07 V and is maintained until $N = 70$. Four peaks are observed in the differential capacity curve of $\text{Fe}_2\text{O}_3/\text{C}/\text{CNT}$ for $N = 1$: two broad peaks at 0.97 and 0.63 V and two smaller peaks at 0.80 and 0.86 V, with slightly varying intensities (Fig. 7d). The low intensity of the peaks in the differential capacity curve of $\text{Fe}_2\text{O}_3/\text{C}/\text{CNT}$ contrasts with the sharp and high-intensity peaks observed for Fe_2O_3 and $\text{Fe}_2\text{O}_3/\text{CNT}$. At a lower voltage, the differential capacity values of Fe_2O_3 and $\text{Fe}_2\text{O}_3/\text{CNT}$ are smaller and stable, while that of $\text{Fe}_2\text{O}_3/\text{C}/\text{CNT}$ presents a sudden increase in magnitude. These results are consistent with the discharge profiles of Fe_2O_3 and $\text{Fe}_2\text{O}_3/\text{CNT}$, which present flat plateau regions at 0.83 and 0.87 V owing to rapid conversion and Li-ion storage, respectively. Thereafter, a sharp decrease in voltage is observed, which yields a small capacity (see Fig. 6b-c). Moreover, the voltage is gradually decreased for the $\text{Fe}_2\text{O}_3/\text{C}/\text{CNT}$ sample, and a significant increase in capacity is observed between 0.5 and 0.01 V (see Fig. 6d).

A pure carbon sample was prepared by annealing a PVP film in an Ar environment. The initial concentration of Fe_2O_3 was varied from 1.2 to 1.4 and 1.8 g. These various Fe_2O_3 concentrations in 40 mL of the DMF/PAN solution were used to prepare LIB electrodes. The electrochemical tests of the four samples (i.e., pure carbon, 1.2- Fe_2O_3 , 1.4- Fe_2O_3 , and 1.8- Fe_2O_3) were performed at the current rates of 100, 200, 500, and 1000 $\text{mA}\cdot\text{g}^{-1}$. The current rate was increased every $N = 10$ cycles until reaching 1000 $\text{mA}\cdot\text{g}^{-1}$, as shown in Fig. S4. The comparison of Fig. S4 and Fig. 8a indicates that the pure carbon electrode had a lower specific capacity than that of pure CNT. The first discharge capacity of the pure carbon anode was 554 $\text{mA}\cdot\text{h}\cdot\text{g}^{-1}$ at a current rate of

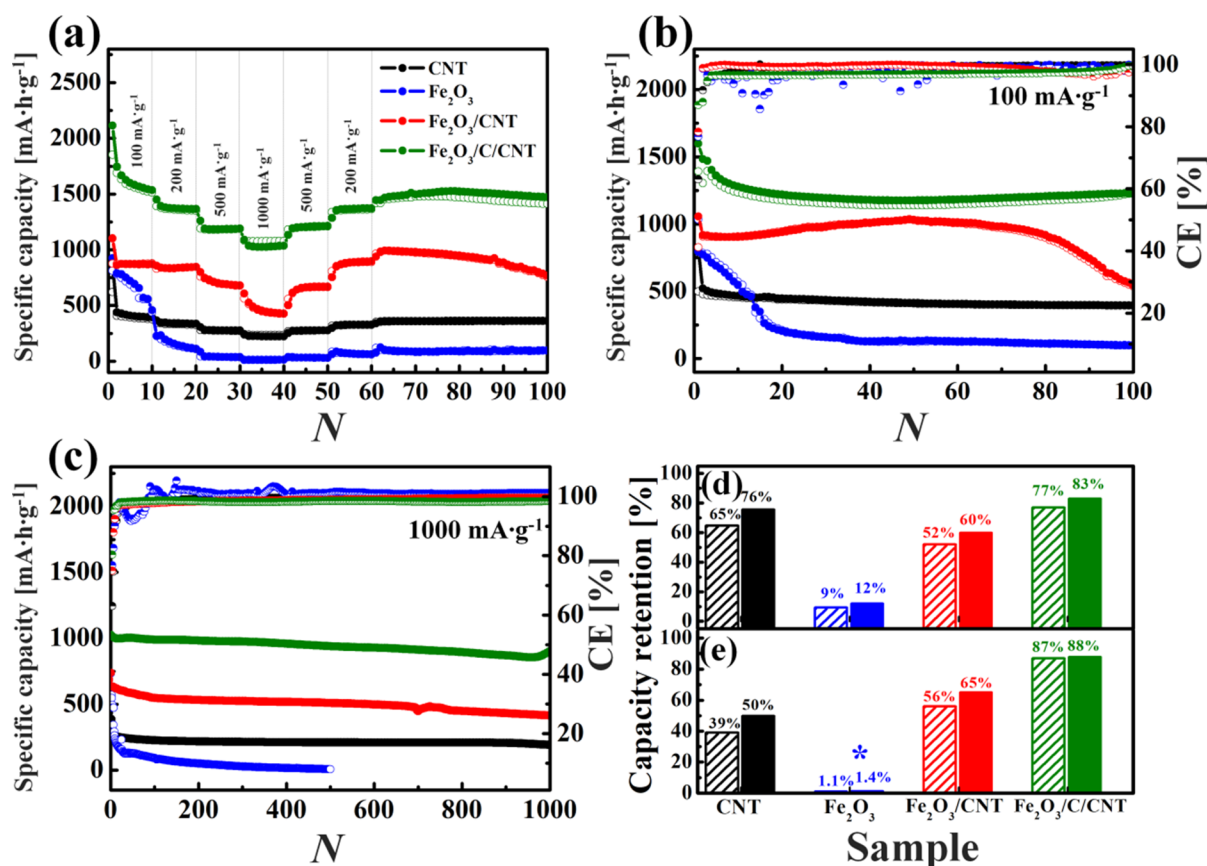


Fig. 8. Electrochemical performances of various samples: (a) rate capability, long-term cycling at (b) low current density ($100 \text{ mA}\cdot\text{g}^{-1}$) and (c) high current density ($1000 \text{ mA}\cdot\text{g}^{-1}$). Capacity retention (%) at (d) low current density ($100 \text{ mA}\cdot\text{g}^{-1}$) and (e) high current density ($1000 \text{ mA}\cdot\text{g}^{-1}$). The dashed and solid column bars indicate the retained capacities for the first and second cycles, respectively. Here, CE is the coulombic efficiency.

$100 \text{ mA}\cdot\text{g}^{-1}$. After $N = 30$ cycles, the current density was increased to $1000 \text{ mA}\cdot\text{g}^{-1}$, at which the capacity was reduced to $172 \text{ mA}\cdot\text{h}\cdot\text{g}^{-1}$. Fig. S4 also shows that the first discharge capacities of 570 , 706 , and $776 \text{ mA}\cdot\text{h}\cdot\text{g}^{-1}$ for the $1.2\text{-Fe}_2\text{O}_3$, $1.4\text{-Fe}_2\text{O}_3$, and $1.8\text{-Fe}_2\text{O}_3$ samples, respectively, were greatly reduced after a few cycles. This rapid deterioration in capacity was attributed to the relatively large Fe_2O_3 particles because the Li-ion insertion/extraction processes were relatively slower for larger particles. The larger particles were also more easily pulverized because the expansion and contraction processes occurred over greater bulk volumes. In addition, the larger Fe_2O_3 particles were subjected to more frequent pulverization because of the greater volume change during the discharging/charging cycles. In such cases, the pulverized particles were more likely to agglomerate during the electrochemical reactions, eventually leading to cracks in the SEI layer, as shown in Fig. S5f. [47]

The specific capacities of the CNT, Fe_2O_3 , $\text{Fe}_2\text{O}_3/\text{CNT}$, and $\text{Fe}_2\text{O}_3/\text{C}/\text{CNT}$ samples are determined at the current rates of 100 , 200 , 500 , and $1000 \text{ mA}\cdot\text{g}^{-1}$. The current rate was increased every 10 cycles until reaching $1000 \text{ mA}\cdot\text{g}^{-1}$. Afterward, the current rate was decreased again to $100 \text{ mA}\cdot\text{g}^{-1}$, as illustrated in Fig. 8a, and was then maintained until the $N = 100$ th cycle. The specific capacities of the CNT, Fe_2O_3 , $\text{Fe}_2\text{O}_3/\text{CNT}$, and $\text{Fe}_2\text{O}_3/\text{C}/\text{CNT}$ samples are 854 , 923 , 1101 , and $2115 \text{ mA}\cdot\text{h}\cdot\text{g}^{-1}$, respectively, at the current rate of $100 \text{ mA}\cdot\text{g}^{-1}$. In addition, the discharge capacities of the CNT, Fe_2O_3 , $\text{Fe}_2\text{O}_3/\text{CNT}$, and $\text{Fe}_2\text{O}_3/\text{C}/\text{CNT}$ samples are 223 , 11 , 426 , and $1035 \text{ mA}\cdot\text{h}\cdot\text{g}^{-1}$, respectively, at the current rate of $1000 \text{ mA}\cdot\text{g}^{-1}$ after 40 cycles. The corresponding capacities of $\text{Fe}_2\text{O}_3/\text{C}/\text{CNT}$ at the $N = 11$ th, 21 st, and 31 st cycles (current rates of 200 , 500 , and $1000 \text{ mA}\cdot\text{g}^{-1}$, respectively) are 1451 , 1261 , and $1090 \text{ mA}\cdot\text{h}\cdot\text{g}^{-1}$. Furthermore, the retained capacities of $\text{Fe}_2\text{O}_3/\text{C}/\text{CNT}$ after the 40 th, 50 th, and 60 th cycles (corresponding to

the current rates of 1000 , 500 and $200 \text{ mA}\cdot\text{g}^{-1}$) are 1035 , 1214 , and $1372 \text{ mA}\cdot\text{h}\cdot\text{g}^{-1}$, respectively, which indicates the superior current capability of $\text{Fe}_2\text{O}_3/\text{C}/\text{CNT}$ compared to those of Fe_2O_3 and $\text{Fe}_2\text{O}_3/\text{CNT}$. This is because the Fe_2O_3 particles are smaller than the as-purchased ones, surrounded by C, and decorated on CNTs. Hence, we further tested the long-term cycling performances of these samples at a low constant current and the high constant current rates of 100 and $1000 \text{ mA}\cdot\text{g}^{-1}$, as illustrated in Fig. 8b and c, respectively. The CE values of CNT, $\text{Fe}_2\text{O}_3/\text{CNT}$, and $\text{Fe}_2\text{O}_3/\text{C}/\text{CNT}$ are initially small but quickly reach approximately 100% (Fig. 8a). However, the CE of Fe_2O_3 fluctuates significantly with almost every change in the current rate. This is attributed to the breaking and reformation of the SEI layers. The generation of cracks is attributed to the pulverization of Fe_2O_3 particles and/or an increase in the insertion or extraction of Li-ions (owing to the changes in current rate).

The excellent stability of the CNT sample is confirmed by the long-term cycling performance data: 76% of the capacity recorded for the first reversible cycle is retained after $N = 100$ cycles (Fig. 8b). However, the capacity of the Fe_2O_3 sample is decreased significantly: the capacity is reduced to $\sim 15\%$ of its initial value within $N = 31$ cycles at the lower current rate of $100 \text{ mA}\cdot\text{g}^{-1}$. Furthermore, at the higher current rate of $1000 \text{ mA}\cdot\text{g}^{-1}$, the capacity of the Fe_2O_3 sample is decreased by 80% within 20 cycles. This is expected and attributed to the low conductivity, volume expansion/contraction, and pulverization occurring during the lithiation/delithiation of the Fe_2O_3 particles. Conversely, the $\text{Fe}_2\text{O}_3/\text{CNT}$ sample exhibits the capacity retention rates of 60% and 65% at the current values of 100 and $1000 \text{ mA}\cdot\text{g}^{-1}$, respectively (Fig. 8d and e). However, the retention is attributed to the breaking of the larger Fe_2O_3 particles during the $\text{Fe}_2\text{O}_3 \rightarrow \text{metallic Fe}$ and $\text{metallic Fe} \rightarrow \text{Fe}_2\text{O}_3$ conversion processes. Such an increase in the

capacity after several cycles could cause instability and unpredictability in the electrochemical performance of the battery. Hence, we synthesized $\text{Fe}_2\text{O}_3/\text{C}/\text{CNT}$ particles using Fe_2O_3 , PVP, and CNTs, as described in Section 2.2, and consequently, we were able to control the unpredictability and instability seen in the $\text{Fe}_2\text{O}_3/\text{CNT}$ composite case. The electrochemical performance of the $\text{Fe}_2\text{O}_3/\text{C}/\text{CNT}$ sample is stable (Fig. 8b and c). In addition, the capacity retention rates of the $\text{Fe}_2\text{O}_3/\text{C}/\text{CNT}$ sample relative to the first cycle and first reversible discharge cycle are almost equal after long-term cycling for the low and high current values of 100 and 1000 $\text{mA}\cdot\text{g}^{-1}$ (Fig. 8d and e, respectively). The CNT, Fe_2O_3 , $\text{Fe}_2\text{O}_3/\text{CNT}$, and $\text{Fe}_2\text{O}_3/\text{C}/\text{CNT}$ samples retain 65%, 9%, 52%, and 77%, respectively, of their capacities for $N = 1$ and 76%, 12%, 60%, and 83%, respectively of the first reversible capacity ($N = 2$) at the low current value of 100 $\text{mA}\cdot\text{g}^{-1}$ (Fig. 8d). Therefore, the capacity retention is improved for all samples as the significant irreversible losses attributed to the formation of the SEI layer are eliminated after the first discharge/charge cycle. The $N = 1000$ discharge/charge cycles are performed to demonstrate the electrochemical stabilities of the samples at the severe current rate of 1000 $\text{mA}\cdot\text{g}^{-1}$. The long-term cycling performance is shown in Fig. 8c, and the capacity retention values are presented in Fig. 8e. The CNT, $\text{Fe}_2\text{O}_3/\text{CNT}$, and $\text{Fe}_2\text{O}_3/\text{C}/\text{CNT}$ samples retained 39%, 56%, and 87% of their $N = 1$ capacities and 50%, 65%, and 88% of their $N = 2$ first reversible capacity. However, the long-term cycle for the Fe_2O_3 sample was carried out only up to $N = 500$ because its retention was reduced to 1.1% of the capacity at $N = 1$ and 1.5% of the capacity at $N = 2$ (see Fig. 8e). The relatively smaller crystallite size of the $\text{Fe}_2\text{O}_3/\text{C}/\text{CNT}$ sample reduces the degree of pulverization and volume expansion/contraction processes. Thus, the relatively smaller crystallite size of the $\text{Fe}_2\text{O}_3/\text{C}/\text{CNT}$ sample prevents the disintegration of the SEI layer (see Fig. S5) and provides excellent electrochemical stability during long-term cycling, as demonstrated in Fig. 8b and c.

The specific capacities of CNT and pure carbon, C, at a current rate of 100 $\text{mA}\cdot\text{g}^{-1}$ are 790 and 554 $\text{mA}\cdot\text{h}\cdot\text{g}^{-1}$, respectively. The first discharge capacity of the Fe_2O_3 anode is 1034 $\text{mA}\cdot\text{h}\cdot\text{g}^{-1}$ at a current density of 100 $\text{mA}\cdot\text{g}^{-1}$. The $\text{Fe}_2\text{O}_3/\text{C}/\text{CNT}$ sample was prepared using a precipitation method with PVP as a capping agent. As previously mentioned, the crystallite sizes of Fe_2O_3 and $\text{Fe}_2\text{O}_3/\text{C}/\text{CNT}$ are 52.3 and 10.7 nm, respectively. In general, a smaller crystallite size provides a shorter pathway for Li-ion diffusion, facilitating rapid charge transfer through both carbon and CNT. Therefore, the capacity contribution by the presence of $\text{Fe}_2\text{O}_3/\text{C}/\text{CNT}$ with a relatively smaller crystallite size is more significant than that by pure Fe_2O_3 with a larger crystallite size; the smaller crystallites are embedded in the $\text{Fe}_2\text{O}_3/\text{C}/\text{CNT}$ sample. Regarding the estimation of the specific capacity contribution by carbon in the samples, elemental concentrations in Table 2 can be utilized, as suggested by Koo et al. [47]. These estimations are detailed in Eq. (S1), (S2), and (S3). From Fig. 6, the first total discharge capacities of the CNT, Fe_2O_3 , $\text{Fe}_2\text{O}_3/\text{CNT}$ and $\text{Fe}_2\text{O}_3/\text{C}/\text{CNT}$ samples were 790, 1034, 1056, and 1598 $\text{mA}\cdot\text{h}\cdot\text{g}^{-1}$, respectively. While assuming that the first discharge capacity of the CNT sample is the carbon content contribution, the carbon content of 15% in the Fe_2O_3 sample indicates the maximum capacity contribution of $(0.15) \cdot (790 \text{ mA}\cdot\text{h}\cdot\text{g}^{-1}) = 119 \text{ mA}\cdot\text{h}\cdot\text{g}^{-1}$. Similarly, the carbon contents of 39% and 72% in the $\text{Fe}_2\text{O}_3/\text{CNT}$ and $\text{Fe}_2\text{O}_3/\text{C}/\text{CNT}$ samples can contribute the maximum capacities of 307 and 568 $\text{mA}\cdot\text{h}\cdot\text{g}^{-1}$, respectively. Subtracting these maximum capacities contributed by carbon from the total capacity, the capacity shares attributed to the Fe_2O_3 can be estimated as 915, 749 and 1030 $\text{mA}\cdot\text{h}\cdot\text{g}^{-1}$ for the Fe_2O_3 , $\text{Fe}_2\text{O}_3/\text{CNT}$, and $\text{Fe}_2\text{O}_3/\text{C}/\text{CNT}$ samples, respectively.

Fig. S5 compares the morphology of the samples before and after the cyclic testing. While the SEI layer sporadically appears as a smooth surface, rather than a spot of aggregated particles, the SEI layers are visibly shown, particularly in the Fe_2O_3 , $\text{Fe}_2\text{O}_3/\text{CNT}$ and $\text{Fe}_2\text{O}_3/\text{C}/\text{CNT}$ samples in Fig. S5. The first column of images in Fig. S5 represents the surface morphology of the film before the cyclic test. These films were

deposited and annealed before electrochemical testing. In Fig. S5b and c, the SEI layer on the CNT film does not show any sign of cracks even after $N = 1000$ discharging/charging cycles, which confirms the highly stable operation of the CNT film shown in Fig. 8b and c. Pulverization was less prevalent in the pure CNT case, which in turn prevented the disintegration of the SEI layer. As a result, the SEI layer suppressed lithium dendrite formation and protected the separator from damage inflicted by the whiskers, which are “needle-like” projectiles from the dendrites. In addition, the carbonaceous nature of the CNTs facilitates the chemisorption of Li-ions over CNT and the intercalation of Li-ions within the CNTs through sidewall openings, open ends, and between layers of the multi-walled CNTs. The high mechanical strength of the CNTs ensures their structural stability even during chemisorption and intercalation during the lithiation and delithiation processes, respectively [48].

In contrast, the Fe_2O_3 film after $N = 500$ cycles showed evidence of pulverization. Fig. S5f shows the disintegration of the SEI layer, inflicted by the repeated volume expansion and contraction processes. The cross-sectional SEM image (not shown) confirms that the Fe_2O_3 film had a thicker SEI layer the CNT film did. Once the film was disintegrated, SEI layer formation occurred again to fill the cracks; more time was required to fill larger cracks. Consequently, the Li-ion insertion/extraction processes were again slowed. Overall, the pulverization and agglomeration phenomena appeared to be prevalent in the Fe_2O_3 case. As a result, the capacity of the Fe_2O_3 sample was deteriorated, as shown in Fig. 8c and e.

However, by adding CNTs to the Fe_2O_3 , the pulverization and agglomeration processes were substantially reduced; see Fig. S5. Fe_2O_3 particles intermingled with CNTs and thus were protected from pulverization and subsequent agglomeration. The CNT network physically and chemically protected the Fe_2O_3 particles from disintegration, although not perfectly. As in Fig. S5i, disintegrations or cracks still appeared in the $\text{Fe}_2\text{O}_3/\text{CNT}$ sample. Agglomeration was significantly reduced in the $\text{Fe}_2\text{O}_3/\text{CNT}$ sample; compare Fig. S5e and h. Therefore, the capacity was sustained for long-term cycling, as evidently shown in Fig. 8c.

As for the $\text{Fe}_2\text{O}_3/\text{C}/\text{CNT}$ sample, the capacity stability was further improved as compared to the other samples; see Fig. 8b and c. The after-cycling SEM images of the $\text{Fe}_2\text{O}_3/\text{C}/\text{CNT}$ sample in Fig. S5k and l show no sign of cracks. Adding carbon via PVP as a capping agent during the synthesis illustrated in Scheme 1 produced smaller Fe_2O_3 particles in the $\text{Fe}_2\text{O}_3/\text{C}/\text{CNT}$ sample, which in turn improved both the capacity performance and stability. In summary, the gradual improvement in the capacity retention from Fe_2O_3 to CNT, $\text{Fe}_2\text{O}_3/\text{CNT}$, and $\text{Fe}_2\text{O}_3/\text{C}/\text{CNT}$, as shown in Fig. 8e, is consistent with the SEM images shown in Fig. S5.

We have also confirmed the electrochemical stability of the $\text{Fe}_2\text{O}_3/\text{C}/\text{CNT}$ sample based on the XRD and TEM data. The XRD data in Fig. S6a indicates that the crystallinity of Fe_2O_3 is retained even after $N = 1000$ discharging/charging cycles under the high current density of 1000 $\text{mA}\cdot\text{g}^{-1}$. The XRD peaks marked with black circles in Fig. S6a arise from Fe_2O_3 , matching well with JCPDS card no. 87-1164. The peaks at $2\theta = 20^\circ$ and 25° indicate the presence of carbon. The two peaks at $2\theta = 50^\circ$ and 75° represent copper. In Fig. S6b, the TEM image of the $\text{Fe}_2\text{O}_3/\text{C}/\text{CNT}$ sample after $N = 1000$ cycles is shown. The red circle indicates the focused area for the HR-TEM and SAED pattern. The HR-TEM image shows the (1 1 0) plane in Fig. S6c while the SAED pattern indicates the (0 2 4) plane of Fe_2O_3 in Fig. S6d.

Electrochemical impedance spectroscopy (EIS) testing was performed in a potentiostatic mode for all the samples in a half-cell configuration. The open-circuit voltage of the assembled half-cell with 24 h aging was $\sim 3 \text{ V}$ vs. Li/Li^+ . The Nyquist spectra for various samples were obtained against Li/Li^+ as a reference/counter electrode. During the EIS analysis (a non-destructive analysis method), a sinusoidal potential wave with the amplitude of 10 mV as minimal perturbation was applied, and the frequency was varied from 100 kHz to 0.01 Hz. The

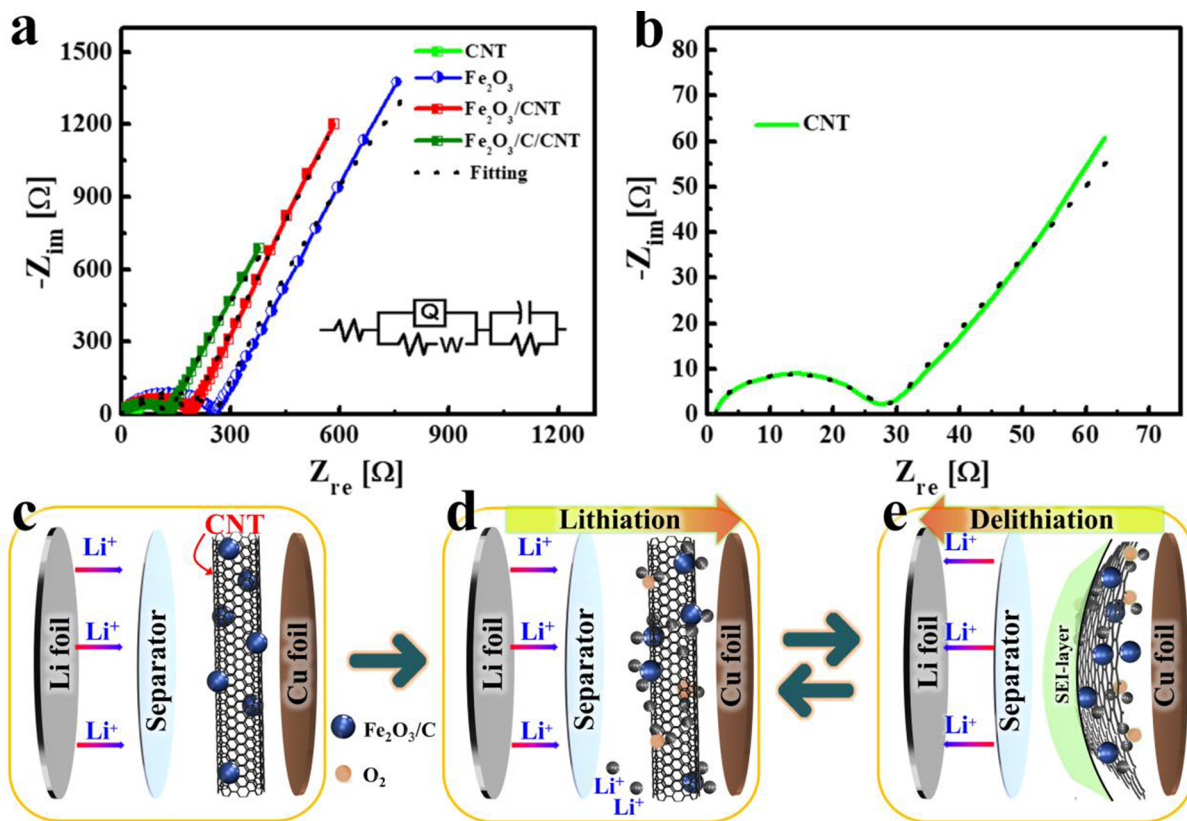


Fig. 9. Electrochemical impedance spectroscopy analysis: (a) Nyquist plot (inset: equivalent circuit). (b) Nyquist plot for pristine carbon nanotube (CNT) sample. Schematic mechanism of lithiation/delithiation for $\text{Fe}_2\text{O}_3/\text{C}/\text{CNT}$: (c) just-assembled, (d) lithiated, and (e) delithiated half-cell. Here SEI is the solid electrolyte interface.

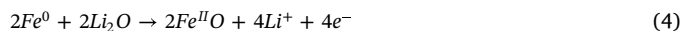
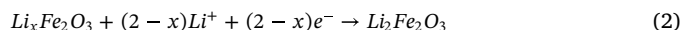
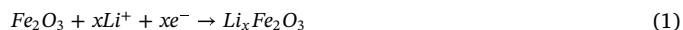
impedance and frequency relationship was well established and expressed as:

$Z(\omega) = |Z| e^{i\theta}$ and $|Z| = \sqrt{Z_{re}^2 + Z_{im}^2}$, where $Z(\omega)$ is the impedance of the electrochemical system (half-cell), $|Z|$ is the modulus of the impedance, θ is the phase corresponding to the frequency, and Z_{re} and Z_{im} are the real and imaginary components of the impedance, respectively. Although a direct relationship existed between the impedance and frequency, the characteristic semicircles and slopes of the Nyquist plots indicated the relationship between Z_{im} and Z_{re} for the specific electrochemical reaction in the system.

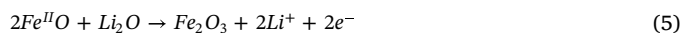
The Nyquist plots in Fig. 9a illustrate the charge transfer and diffusion of Li^+ for various samples. The initial values of the semicircles in the high-frequency region represent the surface resistance (R_s) values at the electrode/electrolyte interfaces of the samples, and the diameters of the semicircles represent the charge-transfer resistance (R_{ct}) values of the samples. The ascending lines following the semicircles in the low- to medium-frequency values represent the diffusion of Li^+ . The R_s and R_{ct} values for each sample are determined after fitting the Nyquist plot data using Randle equivalent circuits (inset of Fig. 9a) and the results are summarized in Table S1. The dotted lines in Fig. 9a represent the fittings for each sample. The Nyquist plot of the pristine CNT sample is also presented separately in Fig. 9b, as it is not distinguishable in Fig. 9a because of the overlap with the data for the other samples. The semicircle in the plot for the CNT sample is the smallest, confirming its excellent conductivity. Conversely, the diameter of the semicircle of the Fe_2O_3 sample (or its R_{ct} value) is larger than those of all other samples because it has the lowest conductivity, which is attributed to its negligible carbon content. The charge transfer capability of $\text{Fe}_2\text{O}_3/\text{CNT}$ is higher than that of Fe_2O_3 because of the CNT incorporation; therefore, the diameter of the semicircle of the $\text{Fe}_2\text{O}_3/\text{CNT}$ sample is smaller than that of Fe_2O_3 . Furthermore, the semicircle of the synthesized $\text{Fe}_2\text{O}_3/\text{C}/$

CNT sample is even smaller than that of the $\text{Fe}_2\text{O}_3/\text{CNT}$ sample because C covers the Fe_2O_3 particles (Fig. S1a and b).

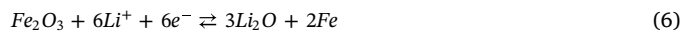
Fig. 9c depicts the just-assembled half-cell, in which the Li foil and $\text{Fe}_2\text{O}_3/\text{C}/\text{CNT}$ electrodes are electrically insulated using the polymer separator (Celgard 2400). The electrolyte and Li foil provide the required Li^+ for energy storage. After several hours of aging, the assembled half-cell attains the maximum voltage of ~ 3 V. During the discharging of the cell, the electrode is lithiated and electrochemical reactions occur. Li^+ is intercalated with the CNTs, while Fe_2O_3 is converted to Fe^{2+} and Fe^{3+} and lastly to metallic Fe^0 , as illustrated in Fig. 9d and discussed in Section 3 (Figs. 6 and 7). The SEI layer is also formed during lithiation, covering the CNT and Fe_2O_3 particles. The reduction reaction involving the conversion of Fe_2O_3 to metallic Fe^0 and the formation of Fe_2O_3 during the oxidation reaction (see Fig. 9e) can be described as follows: [49]



and



The total reversible reaction, involving six Li-ions altogether, can be summarized as follows:



Six C atoms react with one Li-ion during the reduction reaction, and the total redox reaction that occurs during the intercalation/deintercalation of Li-ions in C/CNT can be expressed as follows [50]:

Table 3

Comparison of reversible capacity, charge capacity, and discharge capacity of various Fe–C composite-based Li-ion battery anodes reported in the literature with those of the anodes analyzed in this study.

Material	Freestanding	CC/DC [mAh·g ⁻¹]	RC [mAh·g ⁻¹] /rate [mA·g ⁻¹]	CN	Refs.
Fe ₂ O ₃ /SWNT-600	No	670/692	1007/200	100	[51]
Fe ₂ O ₃	No	995/1423	1176/100	200	[27]
γ-Fe ₂ O ₃ /CNTs	No	709/972	1187/200	400	[52]
γ-Fe ₂ O ₃ /CNTs	No	633/913	860/500	400	[53]
CNT	Yes	397/899	248/50	372	[54]
Fe ₃ O ₄ /carbon	No	999/1795	1317/100	130	[55]
CNTs/γ-Fe ₂ O ₃ /C	No	890/981	919/100	50	[56]
CNT/α-Fe ₂ O ₃ /C	No	1201/1773	1213/100	60	[57]
α-Fe ₂ O ₃	No	927/1306	968/100	100	[26]
Fe ₂ O ₃ /C/CNT	No	1390/1598	1230/100	100	present

CC: Charge capacity, DC: discharge capacity, RC: reversible capacity, and CN: cycle number.



The above reactions suggest that the presence of the CNTs not only improves the conductivity and facilitates faster charge transport through the composite, but also offers space for the intercalation of Li. Furthermore, the long-term cycling stability of Fe₂O₃/C/CNT is higher than that of the Fe₂O₃/CNT composite because of the lower charge-transfer resistance of the intermingled CNTs and smaller Fe₂O₃ particles of the Fe₂O₃/C/CNT sample. The use of PVP as the capping agent during the synthesis of the Fe₂O₃/C/CNT composite allows control of the size of the Fe₂O₃ particles via the formation of a C layer over the Fe₂O₃ nanoparticles, which inhibits the agglomeration of the synthesized Fe₂O₃ particles and thus increases the electrochemical performance and stability of the composite. We compared the results of this study with data previously reported in the literature (Table 3) and concluded that the supersonically sprayed Fe₂O₃/C/CNT composite exhibited compatible performance and excellent capacity retention.

4. Conclusion

The high Li storage capacity and superior capacity retention of the Fe₂O₃/C/CNT composite were attributed to the facile diffusion of Li⁺ in the composite. The three-dimensional morphology of Fe₂O₃/C/CNT conferred relatively good structural and electrochemical stability and provided shorter diffusion pathways for Li⁺. The Fe₂O₃/C/CNT composite presented excellent charge conductivity; moreover, it achieved a high specific capacity of 1230 mA·h·g⁻¹ and the capacity retention of 83% after *N* = 100 cycles. Our paper reports significant insights into the improved and highly stable electrochemical performance of Fe₂O₃ composites as LIB anodes for energy-storage applications.

Declaration of Competing Interest

The authors declare that they have no known competing financial interests or personal relationships that could have appeared to influence the work reported in this paper.

Acknowledgement

This research was supported by the Technology Development Program to Solve Climate Changes of the National Research Foundation (NRF) funded by the Ministry of Science, ICT & Future Planning (NRF-2016M1A2A2936760) and NRF-2020R1A2C1012838. The authors acknowledge King Saud University, Riyadh, Saudi Arabia, for funding this work through Researchers Supporting Project number (RSP-2019/30)

Appendix A. Supplementary data

Supplementary data to this article can be found online at <https://doi.org/10.1016/j.cej.2020.125018>.

References

- [1] K.V. Kravchik, P. Bhauriyal, L. Piveteau, C.P. Guntlin, B. Pathak, M.V. Kovalenko, High-energy-density dual-ion battery for stationary storage of electricity using concentrated potassium fluorosulfonylimide, *Nat. Commun.* 9 (2018) 4469.
- [2] Q. Yun, L. Li, Z. Hu, Q. Lu, B. Chen, H. Zhang, Layered Transition Metal Dichalcogenide-Based Nanomaterials for Electrochemical Energy Storage, *Adv. Mater.* 32 (2019) 1903826.
- [3] M.-S. Balogun, Z. Wu, Y. Luo, W. Qiu, X. Fan, B. Long, M. Huang, P. Liu, Y. Tong, High power density nitridated hematite (α-Fe₂O₃) nanorods as anode for high-performance flexible lithium ion batteries, *J. Power Sources* 308 (2016) 7–17.
- [4] C. Zhang, S. Liu, Y. Qi, F. Cui, X. Yang, Conformal carbon coated TiO₂ aerogel as superior anode for lithium-ion batteries, *Chem. Eng. J.* 351 (2018) 825–831.
- [5] E. Samuel, J.-G. Lee, B. Joshi, T.-G. Kim, M.-W. Kim, I.W. Seong, W.Y. Yoon, S.S. Yoon, Supersonic cold spraying of titania nanoparticles on reduced graphene oxide for lithium ion battery anodes, *J. Alloys Compd.* 715 (2017) 161–169.
- [6] D. Sun, Y. Tang, D. Ye, J. Yan, H. Zhou, H. Wang, Tuning the morphologies of MnO/C hybrids by space constraint assembly of Mn-MOFs for high performance Li ion batteries, *ACS Appl. Mater. Interfaces* 9 (2017) 5254–5262.
- [7] E. Samuel, H.S. Jo, B. Joshi, S. An, H.G. Park, Y.I. Kim, W.Y. Yoon, S.S. Yoon, Decoration of MnO nanocrystals on flexible freestanding carbon nanofibers for lithium ion battery anodes, *Electrochim. Acta* 231 (2017) 582–589.
- [8] Y. Cheng, Z. Yi, C. Wang, Y. Wu, L. Wang, Controllable fabrication of C/Sn and C/SnO/Sn composites as anode materials for high-performance lithium-ion batteries, *Chem. Eng. J.* 330 (2017) 1035–1043.
- [9] B. Joshi, E. Samuel, Y.I. Kim, M.-W. Kim, H.S. Jo, M.T. Swihart, W.Y. Yoon, S.S. Yoon, Hierarchically designed ZIF-8-derived Ni@ZnO/carbon nanofiber freestanding composite for stable Li storage, *Chem. Eng. J.* 351 (2018) 127–134.
- [10] J. Li, D. Yan, S. Hou, T. Lu, Y. Yao, D.H. Chua, L. Pan, Metal-organic frameworks derived yolk-shell ZnO/NiO microspheres as high-performance anode materials for lithium-ion batteries, *Chem. Eng. J.* 335 (2018) 579–589.
- [11] B. Joshi, E. Samuel, M.-W. Kim, S. Park, M.T. Swihart, W.Y. Yoon, S.S. Yoon, Atomic-layer-deposited TiO₂-SnZnO/carbon nanofiber composite as a highly stable, flexible and freestanding anode material for lithium-ion batteries, *Chem. Eng. J.* 338 (2018) 72–81.
- [12] B. Joshi, E. Samuel, H.S. Jo, Y.-I. Kim, S. Park, M.T. Swihart, W.Y. Yoon, S.S. Yoon, Carbon nanofibers loaded with carbon nanotubes and iron oxide as flexible freestanding lithium-ion battery anodes, *Electrochim. Acta* 253 (2017) 479–488.
- [13] L. Hou, R. Bao, D. Kiong Denis, X. Sun, J. Zhang, F. uz Zaman, C. Yuan, Synthesis of ultralong ZnFe₂O₄@ polypyrrole nanowires with enhanced electrochemical Li-storage behaviors for lithium-ion batteries, *Electrochim. Acta* 306 (2019) 198–208.
- [14] B. Joshi, E. Samuel, T.-G. Kim, C.-W. Park, Y.-I. Kim, M.T. Swihart, W.Y. Yoon, S.S. Yoon, Supersonically spray-coated zinc ferrite/graphitic-carbon nitride composite as a stable high-capacity anode material for lithium-ion batteries, *J. Alloys Compd.* 768 (2018) 525–534.
- [15] B.-Y. Wang, H.-Y. Wang, Y.-L. Ma, X.-H. Zhao, W. Qi, Q.-C. Jiang, Facile synthesis of fine Zn₂SnO₄ nanoparticles/graphene composites with superior lithium storage performance, *J. Power Sources* 281 (2015) 341–349.
- [16] T.-G. Kim, E. Samuel, B. Joshi, C.-W. Park, M.-W. Kim, M.T. Swihart, W.Y. Yoon, S.S. Yoon, Supersonically sprayed rGO–Zn₂SnO₄ composites as flexible, binder-free, scalable, and high-capacity lithium ion battery anodes, *J. Alloys Compd.* 766 (2018) 331–340.
- [17] X. Shi, X. Lin, S. Liu, A. Li, X. Chen, J. Zhou, Z. Ma, H. Song, Flake-like carbon coated Mn₂SnO₄ nanoparticles as anode material for lithium-ion batteries, *Chem. Eng. J.* 372 (2019) 269–276.
- [18] H. Zhang, H. Dong, X. Zhang, Y. Xu, J. Fransaer, Cu₂O hybridized titanium carbide with open conductive frameworks for lithium-ion batteries, *Electrochim. Acta* 202 (2016) 24–31.
- [19] J. Qi, Z. Shi, X. Li, B. Gao, H. Wang, L. Yang, Y. Tang, M. Zhu, Pomegranate-like MoC@C composites as stable anode materials for lithium-ion batteries, *J. Alloys Compd.* 786 (2019) 284–291.
- [20] K. Xiang, X. Wang, M. Chen, Y. Shen, H. Shu, X. Yang, Industrial waste silica preparation of silicon carbide composites and their applications in lithium-ion battery anode, *J. Alloys Compd.* 695 (2017) 100–105.
- [21] K. Lee, S. Shin, T. Degen, W. Lee, Y.S. Yoon, In situ analysis of SnO₂/Fe₂O₃/RGO to unravel the structural collapse mechanism and enhanced electrical conductivity for lithium-ion batteries, *Nano Energy* 32 (2017) 397–407.
- [22] M. Sun, M. Sun, H. Yang, W. Song, Y. Nie, S. Sun, Porous Fe₂O₃ nanotubes as advanced anode for high performance lithium ion batteries, *Ceram. Int.* 43 (2017) 363–367.
- [23] T. Jiang, F. Bu, X. Feng, I. Shakir, G. Hao, Y. Xu, Porous Fe₂O₃ nanoframeworks encapsulated within three-dimensional graphene as high-performance flexible anode for lithium-ion battery, *ACS Nano* 11 (2017) 5140–5147.
- [24] X. Chen, Z. Zhao, Y. Zhou, Y. Shu, M. Sajjad, Q. Bi, Y. Ren, X. Wang, X. Zhou, Z. Liu, MWCNTs modified α-Fe₂O₃ nanoparticles as anode active materials and carbon nanofiber paper as a flexible current collector for lithium-ion batteries application, *J. Alloys Compd.* 776 (2019) 974–983.
- [25] Y. Li, Y. Huang, Y. Zheng, R. Huang, J. Yao, Facile and efficient synthesis of α-Fe₂O₃ nanocrystals by glucose-assisted thermal decomposition method and its application

- in lithium ion batteries, *J. Power Sources* 416 (2019) 62–71.
- [26] P. Santhoshkumar, K. Prasanna, Y.N. Jo, I.N. Sivagami, S.H. Kang, C.W. Lee, A facile and highly efficient short-time homogenization hydrothermal approach for the smart production of high-quality α -Fe₂O₃ for rechargeable lithium batteries, *J. Mater. Chem. A* 5 (2017) 16712–16721.
- [27] W. Guo, W. Sun, L.-P. Lv, S. Kong, Y. Wang, Microwave-assisted morphology evolution of Fe-based metal-organic frameworks and their derived Fe₂O₃ nanostructures for Li-ion storage, *ACS Nano* 11 (2017) 4198–4205.
- [28] S. An, B. Joshi, A.L. Yarin, M.T. Swihart, S.S. Yoon, Supersonic cold spraying for energy and environmental applications: one-step scalable coating technology for advanced micro-and nanotextured materials, *Adv. Mater.* 32 (2019) 1905028.
- [29] J.-G. Lee, D.-Y. Kim, B. Kang, D. Kim, H.-E. Song, J. Kim, W. Jung, D. Lee, S.S. Al-Deyab, S.C. James, Nickel–copper hybrid electrodes self-adhered onto a silicon wafer by supersonic cold-spray, *Acta Mater.* 93 (2015) 156–163.
- [30] J.-G. Lee, B.N. Joshi, E. Samuel, S. An, M.T. Swihart, J.S. Lee, Y.K. Hwang, J.-S. Chang, S.S. Yoon, Supersonically sprayed gas-and water-sensing MIL-100 (Fe) films, *J. Alloys Compd.* 722 (2017) 996–1001.
- [31] E. Samuel, T.-G. Kim, C.-W. Park, B. Joshi, M.T. Swihart, S.S. Yoon, Supersonically sprayed Zn₂SnO₄/SnO₂/CNT nanocomposites for high-performance supercapacitor electrodes, *ACS Sustain. Chem. Eng.* 7 (2019) 14031–14040.
- [32] T.-G. Kim, B. Joshi, C.-W. Park, E. Samuel, M.-W. Kim, M.T. Swihart, S.S. Yoon, Supersonically sprayed iron oxide nanoparticles with atomic-layer-deposited ZnO/TiO₂ layers for solar water splitting, *J. Alloys Compd.* 798 (2019) 35–44.
- [33] J.-G. Lee, B.N. Joshi, J.-H. Lee, T.-G. Kim, D.-Y. Kim, S.S. Al-Deyab, I.W. Seong, M.T. Swihart, W.Y. Yoon, S.S. Yoon, Stable high-capacity lithium ion battery anodes produced by supersonic spray deposition of hematite nanoparticles and self-healing reduced graphene oxide, *Electrochim. Acta* 228 (2017) 604–610.
- [34] D.-Y. Kim, J.-J. Park, J.-G. Lee, D. Kim, S.J. Tark, S. Ahn, J.H. Yun, J. Gwak, K.H. Yoon, S. Chandra, Cold spray deposition of copper electrodes on silicon and glass substrates, *J. Therm. Spray Technol.* 22 (2013) 1092–1102.
- [35] J.-G. Lee, D.-Y. Kim, B. Kang, D. Kim, S.S. Al-Deyab, S.C. James, S.S. Yoon, Thin film metallization by supersonic spraying of copper and nickel nanoparticles on a silicon substrate, *Comput. Mater. Sci.* 108 (2015) 114–120.
- [36] J. Wang, M. Gao, H. Pan, Y. Liu, Z. Zhang, J. Li, Q. Su, G. Du, M. Zhu, L. Ouyang, Mesoporous Fe₂O₃ flakes of high aspect ratio encased within thin carbon skeleton for superior lithium-ion battery anodes, *J. Mater. Chem. A* 3 (2015) 14178–14187.
- [37] A. Lassoued, B. Dkhil, A. Gadi, S. Ammar, Control of the shape and size of iron oxide (α -Fe₂O₃) nanoparticles synthesized through the chemical precipitation method, *Results Phys.* 7 (2017) 3007–3015.
- [38] B. Joshi, E. Samuel, M.-W. Kim, K. Kim, T.-G. Kim, M.T. Swihart, W.Y. Yoon, S.S. Yoon, Electrospayed graphene films decorated with bimetallic (zinc-iron) oxide for lithium-ion battery anodes, *J. Alloys Compd.* 782 (2019) 699–708.
- [39] D. Zhang, W. Choi, Y. Oshima, U. Wiedwald, S.-H. Cho, H.-P. Lin, Y. Li, Y. Ito, K. Sugioka, Magnetic Fe@ FeOx, Fe@ C and α -Fe₂O₃ single-crystal nanoblends synthesized by femtosecond laser ablation of Fe in acetone, *Nanomaterials* 8 (2018) 631.
- [40] X. Liu, T. Chen, H. Chu, L. Niu, Z. Sun, L. Pan, C.Q. Sun, Fe₂O₃-reduced graphene oxide composites synthesized via microwave-assisted method for sodium ion batteries, *Electrochim. Acta* 166 (2015) 12–16.
- [41] L. Zuniga, V. Agubra, D. Flores, H. Campos, J. Villareal, M. Alcoutlabi, Multichannel hollow structure for improved electrochemical performance of TiO₂/Carbon composite nanofibers as anodes for lithium ion batteries, *J. Alloys Compd.* 686 (2016) 733–743.
- [42] L. Ji, P. Meduri, V. Agubra, X. Xiao, M. Alcoutlabi, Graphene-based nanocomposites for energy storage, *Adv. Energy Mater.* 6 (2016) 1502159.
- [43] V.A. Agubra, L. Zuniga, D. Flores, J. Villareal, M. Alcoutlabi, Composite nanofibers as advanced materials for Li-ion, Li-O₂ and Li-S batteries, *Electrochim. Acta* 192 (2016) 529–550.
- [44] Z.-H. Yang, H.-Q. Wu, Electrochemical intercalation of lithium into carbon nanotubes, *Solid State Ionics* 143 (2001) 173–180.
- [45] N. Yan, X. Zhou, Y. Li, F. Wang, H. Zhong, H. Wang, Q. Chen, Fe₂O₃ nanoparticles wrapped in multi-walled carbon nanotubes with enhanced lithium storage capability, *Sci. Rep.* 3 (2013) 3392.
- [46] Q. Xiao, Y. Fan, X. Wang, R.A. Susantyoko, Q. Zhang, A multilayer Si/CNT coaxial nanofiber LIB anode with a high areal capacity, *Energy Environ. Sci.* 7 (2014) 655–661.
- [47] B. Koo, H. Xiong, M.D. Slater, V.B. Prakapenka, M. Balasubramanian, P. Podsiadlo, C.S. Johnson, T. Rajh, E.V. Shevchenko, Hollow iron oxide nanoparticles for application in lithium ion batteries, *Nano letters* 12 (2012) 2429–2435.
- [48] Y. Yao, J. Zhang, L. Xue, T. Huang, A. Yu, Carbon-coated SiO₂ nanoparticles as anode material for lithium ion batteries, *J. Power Sources* 196 (2011) 10240–10243.
- [49] Z. Zheng, P. Li, J. Huang, H. Liu, Y. Zao, Z. Hu, L. Zhang, H. Chen, M.-S. Wang, D.-L. Peng, High performance columnar-like Fe₂O₃@ carbon composite anode via yolk@ shell structural design, *J. Energy Chem.* 41 (2020) 126–134.
- [50] D. Aurbach, B. Markovsky, I. Weissman, E. Levi, Y. Ein-Eli, On the correlation between surface chemistry and performance of graphite negative electrodes for Li ion batteries, *Electrochim. Acta* 45 (1999) 67–86.
- [51] Y. Wang, J. Guo, L. Li, Y. Ge, B. Li, Y. Zhang, Y. Shang, A. Cao, High-loading Fe₂O₃/SWNT composite films for lithium-ion battery applications, *Nanotechnol.* 28 (2017) 345703.
- [52] M. Hong, Y. Su, C. Zhou, L. Yao, J. Hu, Z. Yang, L. Zhang, Z. Zhou, N. Hu, Y. Zhang, Scalable synthesis of γ -Fe₂O₃/CNT composite as high-performance anode material for lithium-ion batteries, *J. Alloys Compd.* 770 (2019) 116–124.
- [53] X. Lv, J. Deng, B. Wang, J. Zhong, T.-K. Sham, X. Sun, X. Sun, γ -Fe₂O₃@ CNTs anode materials for lithium ion batteries investigated by electron energy loss spectroscopy, *Chem. Mater.* 29 (2017) 3499–3506.
- [54] C. Kang, E. Cha, R. Baskaran, W. Choi, Three-dimensional free-standing carbon nanotubes for a flexible lithium-ion battery anode, *Nanotechnol.* 27 (2016) 105402.
- [55] W. Han, X. Qin, J. Wu, Q. Li, M. Liu, Y. Xia, H. Du, B. Li, F. Kang, Electrospayed porous Fe₂O₃/carbon microspheres as anode materials for high-performance lithium-ion batteries, *Nano Res.* 11 (2018) 892–904.
- [56] X. Jiang, W. Guo, P. Lu, D. Song, A. Guo, J. Liu, J. Liang, F. Hou, CNTs@ γ -Fe₂O₃@ C composite electrode for high capacity lithium ion storage, *Int. J. Hydrogen Energy* 43 (2018) 14027–14033.
- [57] P. Huang, W. Tao, H. Wu, X. Li, T. Yin, Q. Zhang, W. Qi, G. Gao, D. Cui, N-doped coaxial CNTs@ α -Fe₂O₃@ C nanofibers as anode material for high performance lithium ion battery, *J. Energy Chem.* 27 (2018) 1453–1460.